PRINCIPLES OF TRAFFIC ORGANIZATION IN ANT TRANSPORTATION NETWORKS

by

JUSTIN KITTELL

A DISSERTATION

Presented to the Department of Physics
and the Division of Graduate Studies of the University of Oregon
in partial fulfillment of the requirements
for the degree of
Doctor of Philosophy

September 2023

DISSERTATION APPROVAL PAGE

Student: Justin Kittell

Title: Principles of Traffic Organization in Ant Transportation Networks

This dissertation has been accepted and approved in partial fulfillment of the requirements for the Doctor of Philosophy degree in the Department of Physics by:

Ben McMorran	Chair
Robert Schofield	Advisor
Tristan Ursell	Core Member
John Toner	Core Member
Scott Hansen	Institutional Representative

and

Krista Chronister	Vice Provost of Graduate Studies

Original approval signatures are on file with the University of Oregon Division of Graduate Studies.

Degree awarded September 2023

DISSERTATION ABSTRACT

Justin Kittell

Doctor of Philosophy

Department of Physics

September 2023

Title: Principles of Traffic Organization in Ant Transportation Networks

Collectively, a colony of ants can execute complex and highly organized behaviors, not least of which is the formation of ant 'paths' – the steady bidirectional flow of individuals and resources that provides the colony with nutrients. This bidirectionality necessitates the organization of opposing fluxes, with the choice of organizational scheme impacting the energetic efficiency of the colony. In this work, we perform an experimental investigation into the organizational principles employed by the leaf-cutting ant *Atta cephalotes* under varying levels of lateral confinement. We first extract the statistical properties of the unconfined path via automated imaging and analysis. This characterization is a critical first step in understanding the steady state organization resulting from ant behavior alone. We then explore how the behavior and resulting path properties evolve for the same path under different levels of confinement. This analysis reveals direct quantitative evidence of a three-lane structures, as well as simple examples of energetic optimization at critical widths. Finally, we verify the origin of these structures through simulation of a 'null' model for insect behavior, revealing that the organization demonstrated by *Atta cephalotes* foragers under confinement results from changes in individual behavior, not

solely from ant-wall or ant-ant interaction. This analysis provides a framework for understanding the behavioral trends of a natural transportation system in terms of energetic optimization, with potential impacts on the development of autonomous networks in human engineered systems.

CURRICULUM VITAE

NAME OF AUTHOR: Justin Kittell

GRADUATE AND UNDERGRADUATE SCHOOLS ATTENDED:

University of Oregon, Eugene, Oregon, USA
Indiana University, Bloomington, IN, USA

DEGREES AWARDED:

Doctor of Philosophy in Physics, 2023, University of Oregon
Bachelor of Science in Physics, 2017, Indiana University

AREAS OF SPECIAL INTEREST:

Organizational biophysics, energetics, multidimensional spectroscopy

PROFESSIONAL EXPERIENCE:

Graduate Research Assistant, University of Oregon, 2018-2020, 2023
Graduate Teaching Assistant, University of Oregon, 2017-2018, 2020-2023
Physics Demo Room Facilitator, University of Oregon, 2022-2023

GRANTS, AWARDS AND HONORS:

Weiser Graduate Leadership Award, University of Oregon, 2023

PUBLICATIONS:

Heussman, D., Kittell, J., von Hippel, P. H., & Marcus, A. H. (2022). Temperature-dependent local conformations and conformational distributions of cyanine dimer labeled single-stranded–double-stranded DNA junctions by 2D fluorescence spectroscopy. The Journal of Chemical Physics, 156(4).

Heussman, D., Kittell, J., Kringle, L., Tamimi, A., von Hippel, P. H., & Marcus, A. H. (2019). Measuring local conformations and conformational disorder of (Cy3) 2 dimer labeled DNA fork junctions using absorbance, circular dichroism and two-dimensional fluorescence spectroscopy. Faraday discussions, 216, 211-235.

ACKNOWLEDGEMENTS

I would like to thank my advisors, Tristan Ursell and Robert Schofield for their support and guidance through this project. I would also like to acknowledge my committee for their continued engagement in my research, as well as the physics department at the University of Oregon for providing a space to explore new and interesting scientific ideas.

To my parents, for teaching me to question.

To my friends, for leading the way.

To the ants, for everything.

TABLE OF CONTENTS

Chapter Page

LIST OF FIGURES

Figure Page

Figure Page

Figure Page

Figure Page

Figure Page

LIST OF TABLES

Table Page

CHAPTER I

INTRODUCTION

1.1 The Coordinated Motion of Ants

Biological systems in the natural world often consist of many semi-identical, polar, self-propelled individuals interacting at close range. This description can be applied across many orders of magnitude, including bacterial swarms, bird flocks, schools of fish, and herds of wildebeest. Despite the vast differences in scale, there is a tendency for common group movement dynamics to emerge from the instinctual decision making of the many actors. In these examples, individuals tend to align themselves locally with their neighbors while moving forward, resulting in large-scale average alignment and dramatic density fluctuations across the group. This frequently observed 'coordinated motion' (CM) is a common emergent pattern in active matter systems [1]. As the decision making of most animals is guided by an evolved, instinctual 'rule-set' for responding to local stimuli, the prevalence of CM across disparate biological systems is an example of convergent evolution; the globally reduced risk of predation these movement patterns provide

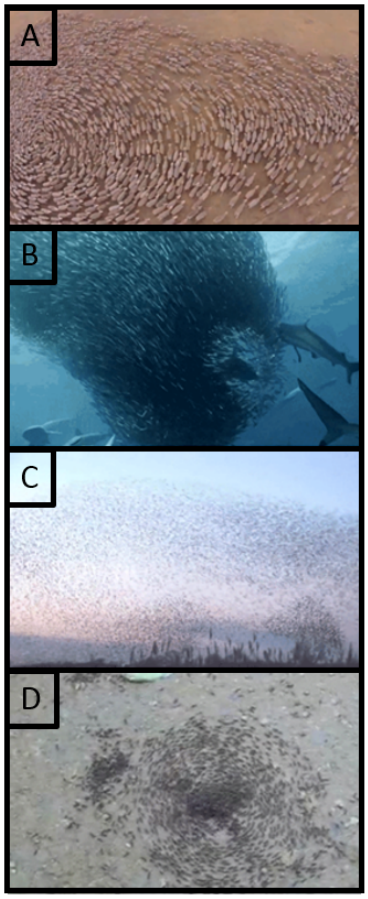

Figure 1. Examples of coordinated motion in (A) a sheep herd, (B) a school of fish, (C) a flock of birds, and (D) an ant colony.

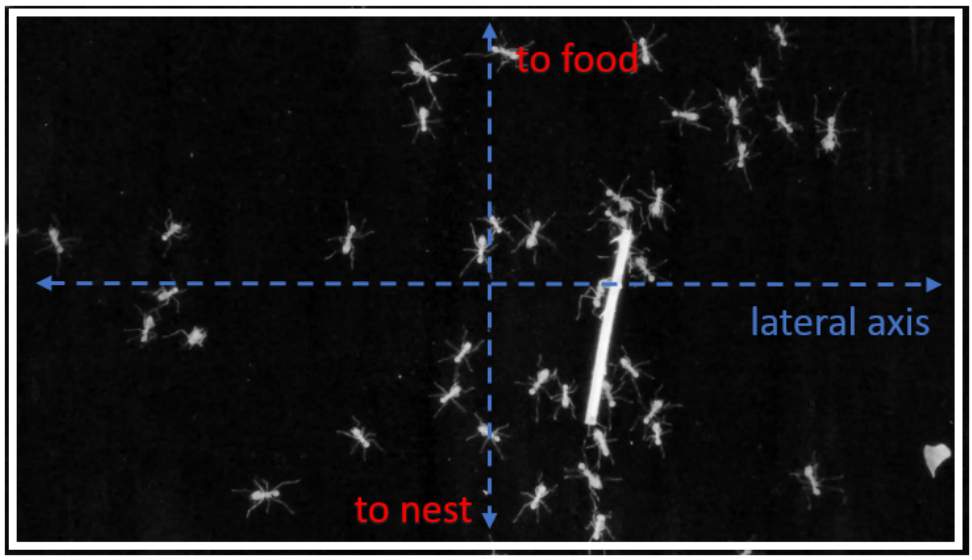

!t

Figure 2. *Atta cephalotes* foragers follow and reinforce stigmergic pheromone signals while transporting organic material, producing a laterally confined band of high ant density along the food-nest axis.

acts as an evolutionary impetus for species to adopt local behavioral strategies that produce them [2].

Though commonly employed for predation avoidance, a unique class of coordinated motion can also be observed in the transportation networks of foraging ants, in which ant-ant interactions and individual decision making confer dramatic global benefits to the colony. Ants, an ecologically dominant species in nearly every terrestrial environment on earth, engage in cooperative behaviors both in and around their nest, directed primarily by chemical signaling [3][4]. While not true for all ants, typically when a foraging ant discovers food far from the colony, it deposits a volatile recruitment pheromone along the ground while returning to the nest; this chemical guides other foragers to the food source. On their return trip, the recruited foragers can reinforce or modify the original path by depositing their own pheromone. This chemotactic navigation strategy generates the characteristic ant 'path', shown

in figure 2, which is the dense, temporally persistent network of foragers frequently observed outside an ant colony.

1.2 Energetic Optimization in a Natural System

While transporting materials under these crowded conditions, the global dynamic evolution of the foraging network is guided entirely by the local interaction rules of individual ants [5][6]. Without any global control, these networks are capable of approximating minimum length paths through both free [7] and spatially confined [8] regions in 2D, as shown in figure 3. As some ant species are known to be energetically limited due to the high energetic cost of transporting and processing materials [3], minimizing overall network length may improve the reproductive fitness of the colony, selecting for instinctual rule-sets which minimize energetic expenditure

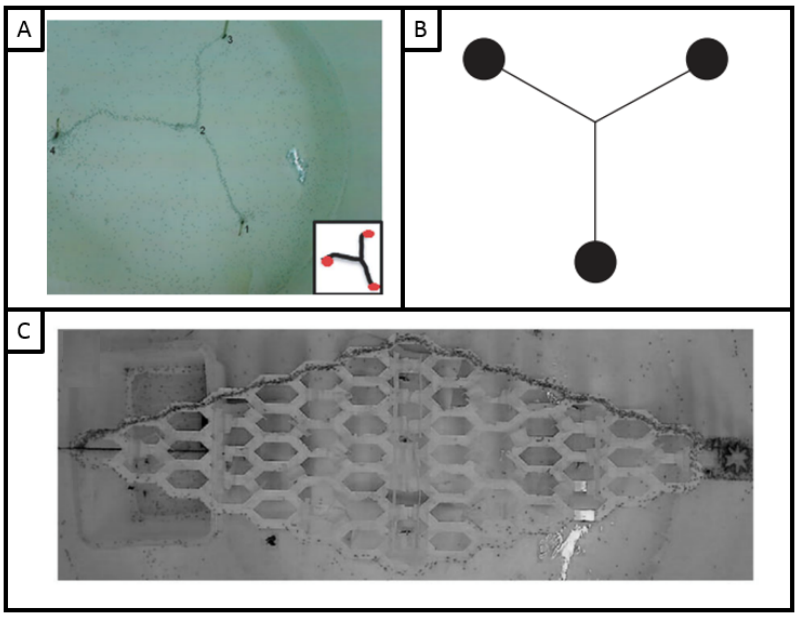

Figure 3. Ant path length minimization. An unconfined ant transport network (A) approximates a minimum length network (B) between three spatially separated ant colony entrances (B) (Latty et al., 2011). (C) Argentinian ants find a minimum length solution to a graph-theoretic representation of the Towers of Hanoi puzzle (Reid et al., 2011)

while maintaining a level of path flexibility and exploration appropriate for the changing conditions of the local environment. This emergent property has inspired novel computer algorithms for minimizing network lengths, commonly referred to as the traveling salesman problems [9]. Generally, these algorithms simulate the movement of many 'ants' through a defined network, while keeping track of recent activity levels at each node. By updating the positions of each ant based on relative 'pheromone concentration' in any direction and connecting nodes along paths of peak activity, algorithms like these find approximate minimum length paths through complex environments. This underscores the potential for other improvements in human designed systems to come from the study of biological transport networks.

In addition to minimum length paths, the collective decision making of many individual ants can produce other network level phenomena like context dependent flux organization. When laden nest-bound foragers meet their unladen food-bound peers on the path, the potential for head-to-head collisions threatens transportation efficiency and necessitates structural organization of the local ant flux perpendicular (lateral) to the direction of traffic flow. The resulting organized ant flux has been shown to display both spatial and temporal organization in bidirectional flow, as shown in figure 4 [10]. One type of spatial organization is 'laning', which arises when incoming and outgoing groups occupy well-defined and separated positions across the path. Biologists have described the observation of 3 lane traffic patterns in some species of ant (*Atta colombica*, *Eciton burchelli*), a structure attributed to differences in the yielding rules between incoming and outgoing ants, exemplified in figure 4A [11]. This investigation aims to present a quantitative measure of the degree of laning exhibited by the ant species *Atta cephalotes* (*A.ceph*) under varying levels of lateral confinement.

When sufficiently confined, interactions between the walls and other ants (referred to here as 'steric' interactions) necessitate temporal organization, or 'platooning', the alternating occupation of a point on the path by groups of ants heading in opposite directions. Like the three-laned structure above, the details of platooning statistics such as platoon size and duration also depend on the rules of interactions between ants, especially yielding, with examples shown in figure 4B. Which organizational strategy emerges in the foraging column explicitly depends on the confined width of the path [10], and while previous experiments have studied

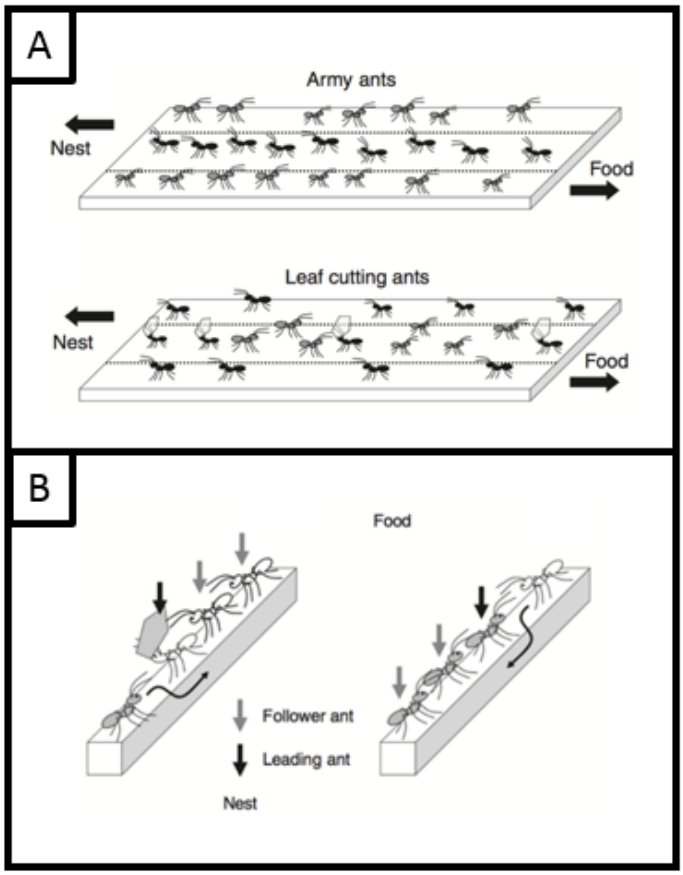

Figure 4. Schematic examples of spatial and temporal organization in ant traffic (Fourcassié et al., 2010). (A) Lane structures observed in the paths of army ants and leaf cutting ants with unique spatial organizations represented by each. (B) Observed yielding behavior for platooning leaf-cutters under lateral confinement.

ant traffic under different confining widths [12][13], no studies have yet explored how the organization of flux dynamically evolves as the confining width is varied. As with the path length minimization above, it is likely that the organizational strategy which emerges in response to these external pressure minimizes some fraction of the colonies energetic expenditure. By smoothly varying the level of steric confinement, we expect to observe dynamic transitions in the organizational strategies employed by the *A.ceph* – an organizational strategy phase transition driven by energetic necessity.

1.3 Models for Coordinated Motion and Extensions to Bidirectional Traffic

To effectively extract energetically optimized rule-sets from the *A.ceph* foraging column, physical models with adjustable behavioral parameters can be tuned to match observations like those made in this study. For coordinated motion in general, two broad classes of models have been employed to describe behaviors observed in biological systems. The Vicsek model is an agent-based simulation that quantitatively connects specific individual rule-sets with observable emergent properties. Under this model, actors have a position vector $r(t)$ and a scalar orientation $\theta\,(t)$ that evolve according to

$$\mathbf{r}_i(t+\delta t) = \mathbf{r}_i(t) + v\Delta t[cos(\theta_i),\ sin(\theta_i)]$$

and

$$\theta_i(t+\delta t) =< \theta_j(t) >_{|r_i - r_j| < r_{min}} + \eta_i(t)$$

Here, v is the constant speed of individual actors, $< \theta_j(t) >_{|r_i - r_j| < r_{min}}$ is the average orientation of all neighbors within a radius r_{min} of the focal actor, and $\eta_i(t)$ is an orientational noise term often equal to zero [1]. These equations encapsulate a simple interaction rule: individuals attempt to align themselves with their neighbors as they move forward. Simulations of this model reproduce the local orientational alignment, density fluctuations, and global movement characteristic of coordinated motion in biological systems. Further, the success of the Vicsek model highlights the ability of simple rule-sets to produce coordinated motion. Increased complexity can be built into agent-based models like this, a strategy employed in other works to explore the glass-like dynamics of ant traffic jams [12]. Their discrete lattice based model contained two groups of actors moving in opposite directions, and included a variable 'interaction time' T_{int}, specifiying the duration of head-to-head interactions. Simulations of this model accurately reproduced the jamming statistics of fire-ants for only certain values of T_{int}, those which matched the measured interaction time for the same species. This result highlights how simulating different behaviors and comparing the structural outputs to observational data can reveal which behavior is best represented in the group. With data sets that include spatial and angular distributions of individuals, expanding models like this to include differences in yielding behavior may allow us to extract principles of efficient traffic organization from organisms like *Atta cephalotes*.

The extraction of these principles from agent-based modeling requires long periods of simulation to provide an effective comparison. As an alternative approach,

encoding behavior into a continuum description can provide direct insight into which behavioral trends result in which global system output. An example of this can be found in the continuum based description of flocking introduced by Toner and Tu in 1998. In this model, the properties of a generalized "flock" are described by a coarse-grained scalar density field $\rho(x,\ t)$ and vector velocity field $\vec{v}(x,\ t)$, which evolve in time according to the Toner-Tu equations

$$\delta_t\vec{v} + \lambda_1(\vec{v}\cdot\vec{\nabla})\vec{v} + \lambda_2(\vec{\nabla}\cdot\vec{v})\vec{v} + \lambda_3\vec{\nabla}(|\vec{v}|^2)$$
$$= \alpha\vec{v} - \beta|\vec{v}|^2\vec{v} - \ \vec{\nabla}\ P(\rho) + D_B\vec{\nabla}(\vec{\nabla}\cdot\vec{v}) + D_T\nabla^2\vec{v} + D_2(\vec{v}\cdot\vec{\nabla})^2\vec{v} + \vec{f},$$
$$P(\rho) = \sum_{n=1}^{\infty}\sigma_n(\rho-\rho_0)^n\ ,\quad \frac{\partial\rho}{\partial t} + \nabla\cdot(\vec{v}\rho) = 0$$

The λ_n terms are the hydrodynamic derivatives of the velocity field, the α and β terms ensure a non-zero velocity in the ordered phase, and the diffusive D_n terms encompass the coupling between neighboring members of the flock. P is the effective pressure of the system, defined in term of density relative to ρ_0, and $\vec{f}$ is a noise term. This equation is analogous to the Navier-Stokes equation but for active (i.e. self-propelled) hydrodynamic systems [1]. Remarkably, by considering the allowed solutions to this equation, Toner and Tu were able to mathematically predict the continuous breaking of rotational symmetry that occurs when active matter systems exhibit global motion. By encapsulating local rule-set interactions into a continuum description of matter, the spontaneous emergence of a global property can be predicted, bypassing the simulation necessary in agent-based approaches.

In order to predict the long term behavior of a bidirectional flow in a human engineered system, including any lateral flux organization, a hydrodynamic

description of counter-propagating density fields may allow us to anticipate the emergence of these trends from encoded behavioral inputs. Surprisingly, flux organization can spontaneously emerge in bidirectional flows consisting of simple molecules, complex plasmas, and driven colloids. The emergence of these structures in flows not guided by behavioral rule-sets hints at a more fundamental mechanism for lane formation, which recent work has explored in the hydrodynamic limit [14]. This work shows that spatial inhomogeneities and gradients in counter-propagating density fields can drive the temporal evolution of these opposing fluxes. This model predicts the instability of homogeneous bidirectional flow, providing a mathematical basis for the nucleation of lanes in systems with and without behavioral rule-sets. These results are derived for symmetric flows, where the yielding characteristics of counter propagating individuals are assumed to be identical. While effective for many pedestrian and automotive models, as well as non-sentient systems like plasmas and colloids, the emergence of the traffic patterns observed in the foraging columns of the *A. ceph* are believed to be a direct consequence of differences in behavior between nest-bound and food-bound ants [11]. While finding a mathematical basis for the steady state flux distributions observed within the ant path would require an extension of this hydrodynamic model, successfully encoding the behavioral characteristics found in this study into an accurate hydrodynamic description would provide a framework for extracting the rule-set parameters evolutionarily encoded in the individual ants. Data-sets like the one utilized in this study may provide the comparison necessary for extracting these behavioral parameters from the simulation of such hydrodynamic models.

1.4 Outline

In this work, we provide quantitative evidence of spatial organization in the foraging column of the leaf-cutting ant *Atta cephalotes* and explore how this lane structure evolves under varying levels of external confinement. We first sample the positions and orientations of foraging ants over many days in the unconfined limit; this allows us to characterize both the natural width of the ant path and observe any steady state lane structure through plots of average directionality and flux correlate in the 'lab frame', a coordinate system defined in figure 5A. We then explore how these measures of organization respond to cyclic changes in the degree of steric confinement. Results are presented for *A.ceph* foragers under moderate (2.5 – 5.0 cm) and heavy (1.0 – 3.5 cm) confinement, allowing us to identify organizational transition points under both compression and expansion.

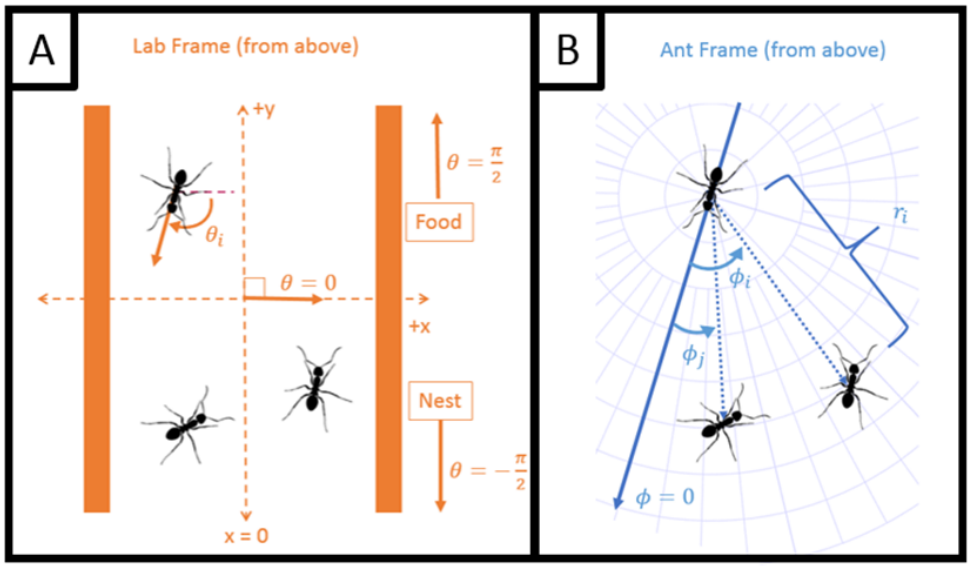

Figure 5. Comparing measurement in the lab frame and the ant frame (A) θ_i gives the angle of the i^{th} ant with respect to the lab coordinate system. A lab frame orientation of 0 or pi is directly perpendicular to the path (B) The same ants represented from the perspective of a single ant, showing the distances and orientations (r and ϕ, respectively) to other ants in the same frame.

In addition, we compute the statistics of ant-ant interactions from the reference frame of each individual to explore the perspective-based density and alignment fields around the 'average' individual in our system, with results presented in the 'ant frame', described in figure 5B. Similar analysis techniques have been employed to study the statistics of collective motion and group alignment in herds of migrating caribou [15], allowing researchers to identify unique social interaction rules for the two species under study. By sorting the *A.ceph* into 2 groups based on lab frame directionality (nest-oriented vs food-oriented) and calculating the average agent-based density and tangent-tangent pair correlations maps for each, we show a width dependent contrast between the social interaction rules of the two groups. By connecting the organizational changes observed in the lab frame with corresponding changes in these agent based maps, this analysis aims to provide a link between average local information and global outcomes in the ant column.

Finally, we compare the statistical lane structures we observe in our system with those produced by a 'null' model to fully explore the degree of self organization the foraging column achieves. Under this simple hypothesis, the positions and orientations of individual ants are selected from uniform distributions, only restricted by steric interactions with physical barriers and other ants. By matching experimental parameters like ant number, confining width, and ant size between our simulated and collected data, we observe how strongly the emergent organizational structure in the ant column differs from the simplest 'null' prediction. This modeling process aims to better differentiate the organizational transitions arising due to changes in ant behavior from those created by physical changes in the apparatus, verifying the origin of any structural transitions as behavioral, not apparatus-dependent.

Ants are but one example of a self-organizing biological system where the rule-sets guiding individual behavior can lead to global benefits. The rule-sets and behavioral principles that shape these transportation networks, and their global properties, may contain useful design principles for human systems with similar spatial or energetic constraints. Although the chemotactic mechanisms that underlie ant behavior have been explored in a biological context, many salient questions about the ants' organization strategies remain poorly understood. This includes the dynamic evolution of the ants' flux distribution, which, as a first goal, this project seeks to illuminate through a combination of environmental control, quantitative imaging, and perspective-based analysis techniques. Revelation of these organizational strategies and their emergence from individual rule-sets will provide key insights into the structure of biological transport networks and may provide a conceptual framework for the design of robust autonomous networks in human transportation systems.

CHAPTER II

STATISTICS OF STEADY-STATE PATH STRUCTURE IN THE UNCONFINED LIMIT

2.1 The 'Unconfined' Path

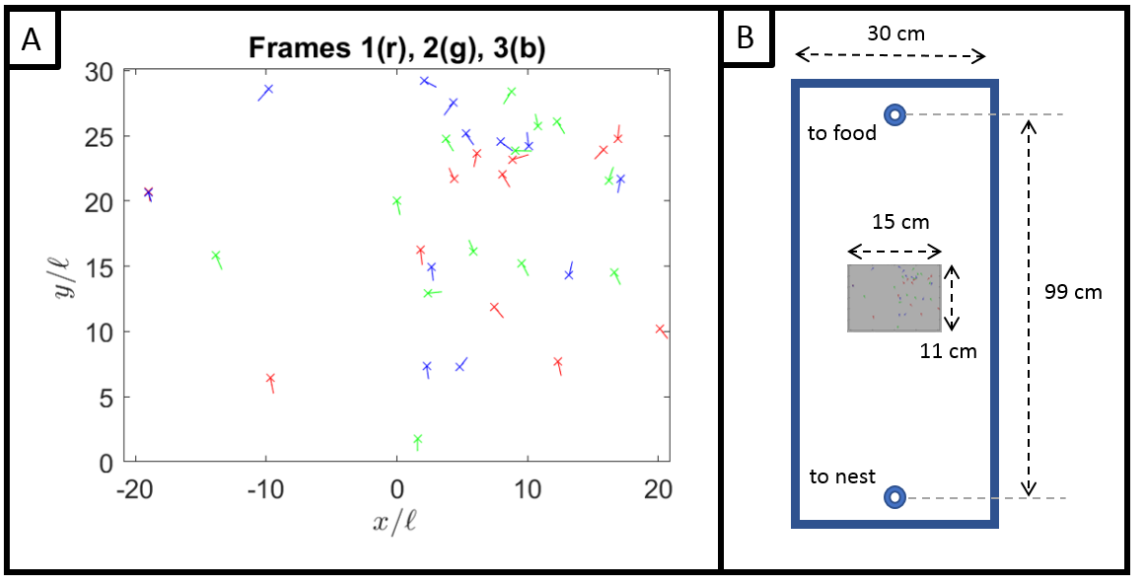

Figure 6. (A) Lab-frame representation of ant position and orientation, marked by Xs and arrows respectively. Positions are given in units of ℓ, the average ant length, where ants with a lateral position of $x = 0$ fall along the minimum length path. Ants from separate video frames are differentiated by color. (B) Top-down view of the sampling region (gray) in context, with relevant length scales shown. Figure not to scale

The foraging column of the *A.ceph* is a dynamic system with network structure and inter-ant properties which vary dramatically over both space and time. Figure 6A shows the positions and orientations of ants in three consecutive frames, collected at 1 FPS, with positions given in units of the average ant length. These position maps reveal dramatic changes in ant density and orientation on a frame-by-frame basis. To explore the statistical properties of this foraging column in the steady state, we must integrate the position and orientation information of individual ants over many such frames. As the auto-chemotactic navigation strategy of the ants

results in a laterally localized band of high density like that exemplified in figure 7A, characterizing the width of this narrow spatial region will define a critical length scale for the ant's transportation network. In this investigation, the path 'width' is taken to be a statistical quantity referring to the average lateral spread of ant locations about their mean x position μ_x which likely corresponds with the location of peak pheromone concentration. In order to quantify this local path property in the steady state, we route the foraging column through a 2D region where the ant path is 'unconfined'. This condition is satisfied when most ants remain far from steric barriers, with the bulk of the ant traffic moving through free space. This prevents steric interactions from impacting the lateral density profile, ensuring any observed structure results from the decision making of the ants alone. Figure 6B shows a schematic of the observation platform utilized in this study, with the sample region indicated in gray. We define the confining width $W_{conf.}$ as the minimum distance between the steric barriers perpendicular to the food-nest axis. For $W_{conf.} = 30cm$, the frequency of ant-wall steric interaction is extremely limited by the energetic cost of the associated path length increase. Under these conditions, the navigation strategy employed by the *A.ceph* foragers results in a mean ant position far from any confining walls, allowing us to observe the unconfined path over long time scales. Exploring the lateral distribution of ant positions under these conditions is necessary as the degree of steric confinement we later impose with physical barriers can only be understood in terms of the spatial distribution of ants across the natural, unconfined path. For the trials presented below, each plot draws on frames collected consistently over 4 days at 1 FPS, averaging distributions from both high and low ant density. Data collection parameters can be found in chapter 5, and a temporal breakdown of ant flux can be found in appendix A.1.

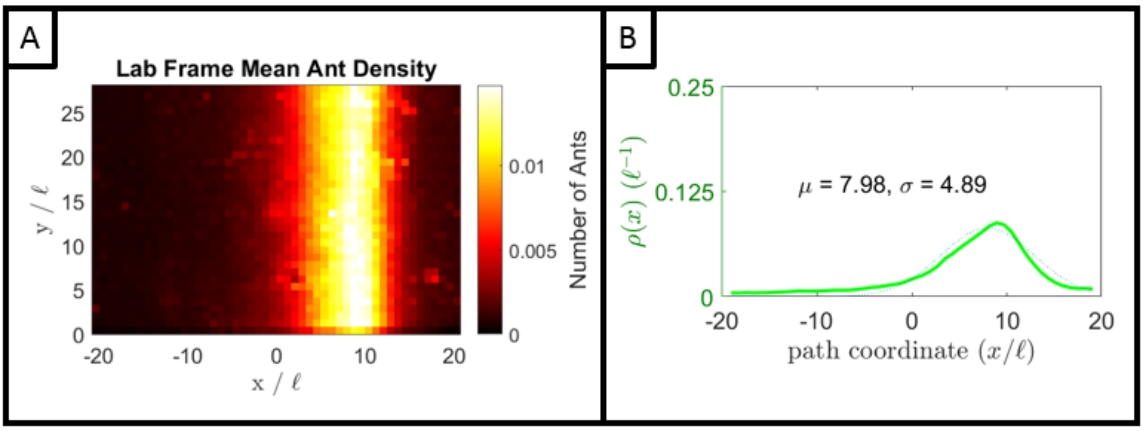

Figure 7. Spatial and Lateral Ant Density in the Lab Frame (A) A spatial heat-map showing average ant number per square ant length (ℓ^{-2}) per frame. Horizontal and vertical positions are given in units of ℓ (B) Lateral density profile, showing the average linear ant density vs. lateral position in ant lengths. The blue curve shows a normal distribution with a mean and standard deviation matching that of the data.

2.2 The Natural Path Width

In Figure 7A, we present the lab frame mean ant density of *A.ceph* foragers for the sample region shown in figure 6B. A lateral position of $x = 0$ marks the location of the straight-line path between the two entrances, with the x axis running perpendicular to the presumed direction of traffic flow. This plot, referred to as a 'heat map', shows the average ant density ($\frac{N}{\ell^2}$) at a given position (x, y) inside the observation region, with higher densities represented by warmer colors. If we assume any lateral structure we observe is independent of our sample location along the ant path, we can collapse the 2-dimensional data represented by figure 7A along its vertical axis, considering only the lateral (horizontal) position of each ant. Under this assumption, we can produce a lateral density plot like the one shown in figure 7B. This plot shows the average linear ant density ($\frac{N}{\ell}$) observed at each lateral position x. We can calculate statistical properties of the resulting distribution to provide an estimate of the 'natural' path width maintained by *Atta cephalotes* under laboratory conditions. For the specific trial shown in figure 7, the lateral mean of the ants'

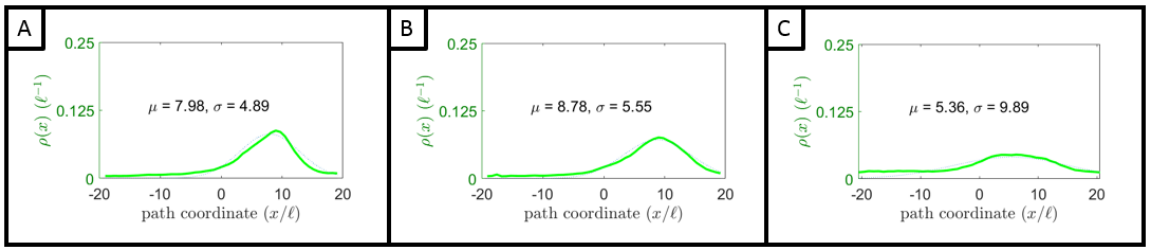

Figure 8. Linear ant density vs. lateral position. (A), (B), and (C) show results from 3 unique data collection periods. The blue curve in each shows a normal distribution with mean and standard deviation matching that of the observed data.

x positions μ_x deviates from the shortest length path ($x = 0$) by 7.98 ant lengths, with a standard deviation of $\sigma_x = 4.89$ ant lengths. We include a scaled Gaussian distribution with the same mean and standard deviation to emphasize any deviation from normalcy present in these lateral distributions. For this trial, the density profile shows a pronounced negative skew.

For all trials, we find the mean standard deviation of ant position to be $\overline{\sigma_x} = 6.7 \pm 2.2\ \ell$, which implies that on average only 32% of ants stray further than 6.7 ± 2.2 ant lengths from the path center. This sets an important length scale for our system, as for all confining widths $W_{conf.} >>> 2\sigma$, we expect the density profile and organization to be largely independent of width, while for $W_{conf.}$ close to $2\sigma_x$ or below, we anticipate that the organizational strategy employed by the ants will strongly depend on the level of confinement. Over all trials, the average lateral deviation of the path center (determined by μ_x) from the shortest, straight-line path at $x = 0$ is approximately 7.4 ± 1.4 ant lengths. While this lateral deviation is persistent over the timescales explored in this study (96 hours) necessitating a small increase in the ant's energy expenditure compared to travel along the minimum-length path, the lateral deviation is very small compared to the total distance between input ports, which for our system is greater than 250 ℓ. Given the small change in total length caused by this lateral

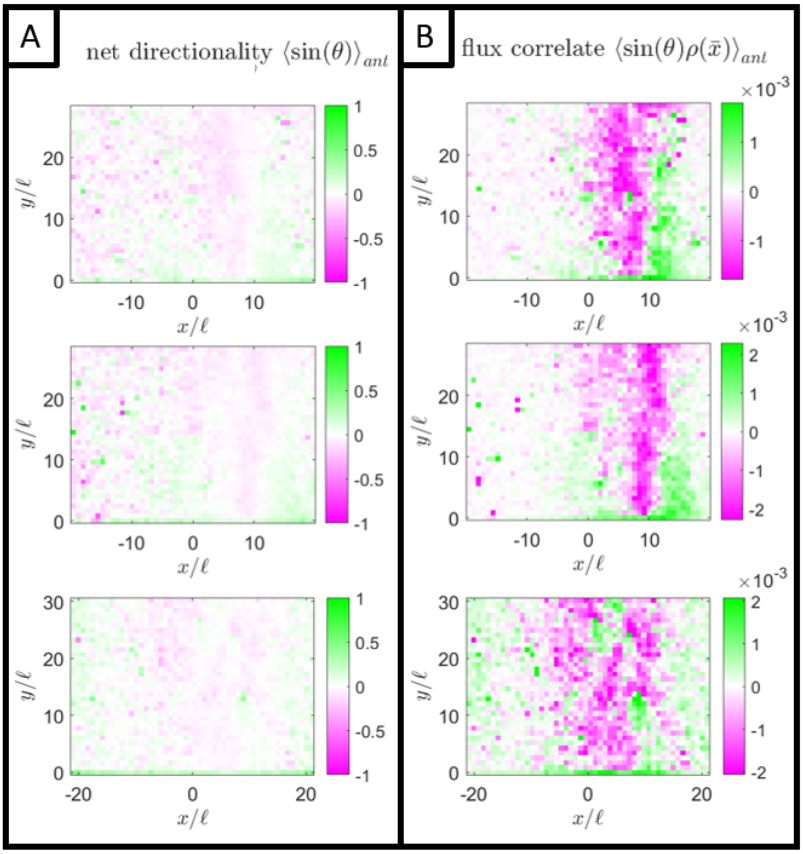

Figure 9. Ant Direction in the Lab Frame (A) Net directionality as a function of lab frame position (x, y) in units of ℓ, provided for the same 3 trials as above. Bin color represents the average projection of the orientation vectors in each bin onto the food-nest axis (B) Flux correlate, the product of net directionality and average ant density in the lab frame. This emphasizes the regions of highest net flux.

deviation, it is unlikely that any minimization procedure which emerges from the behavior of the *A.ceph* foragers would be sensitive to such a small deviation from the shortest path. Surprisingly, the path established by the ants always maintained a positive μ_x, with the ant path always drifting slightly to the right in the lab frame. This reproducibility suggests such lateral drift may result from an innate behavioral mechanism which further studies may illuminate.

2.3 Lab Frame Directionality

While the analysis so far has focused only on the lateral position of the ants, including orientation information allows us to estimate the steady state flux distribution of the unconfined foraging column. In our analysis, θ refers to the angle of an ant in the lab frame as defined in figure 5A, with $\pi > \theta > -\pi$ and $\theta = \frac{\pi}{2}$ corresponding to ants oriented away from the colony. In order to identify regions in our observation window with a preferred direction of travel, we bin the *A.ceph* in 2D based on their (x, y) positions and report the average projection of the ants' orientation vector on the food-nest axis ($< sin(\theta_i) >$) in each bin. Figure 9A shows these plots of 'net directionality' for the same three trials shown above, in which we can identify regions which show a persistent tendency for food-bound or nest-bound travel. Regions more likely to be occupied by nest-bound ants are magenta, while regions more likely to be occupied by food-bound ants are green. In order to emphasize the regions which contribute most to the total flux, we take the product of the net-directionality with the spatial density, yielding a quantity referred to as the 'flux correlate' (FC), shown in figure 9B. On these plots, temporally persistent lanes appear as vertical bands of contiguous bright colors. While such regions appear in our analysis, in the next section we will attempt to characterize the emergent organization perpendicular to the direction of travel, which may have the largest impact on the energetic efficiency of the colony.

.

2.4 The Fundamental Laning Diagram (FLD) and the Lateral Dependence of the Flux Correlate (FC)

As described above, if we assume that over the vertical extent of our observation region the distribution of orientations are constant, we can ignore spatial information

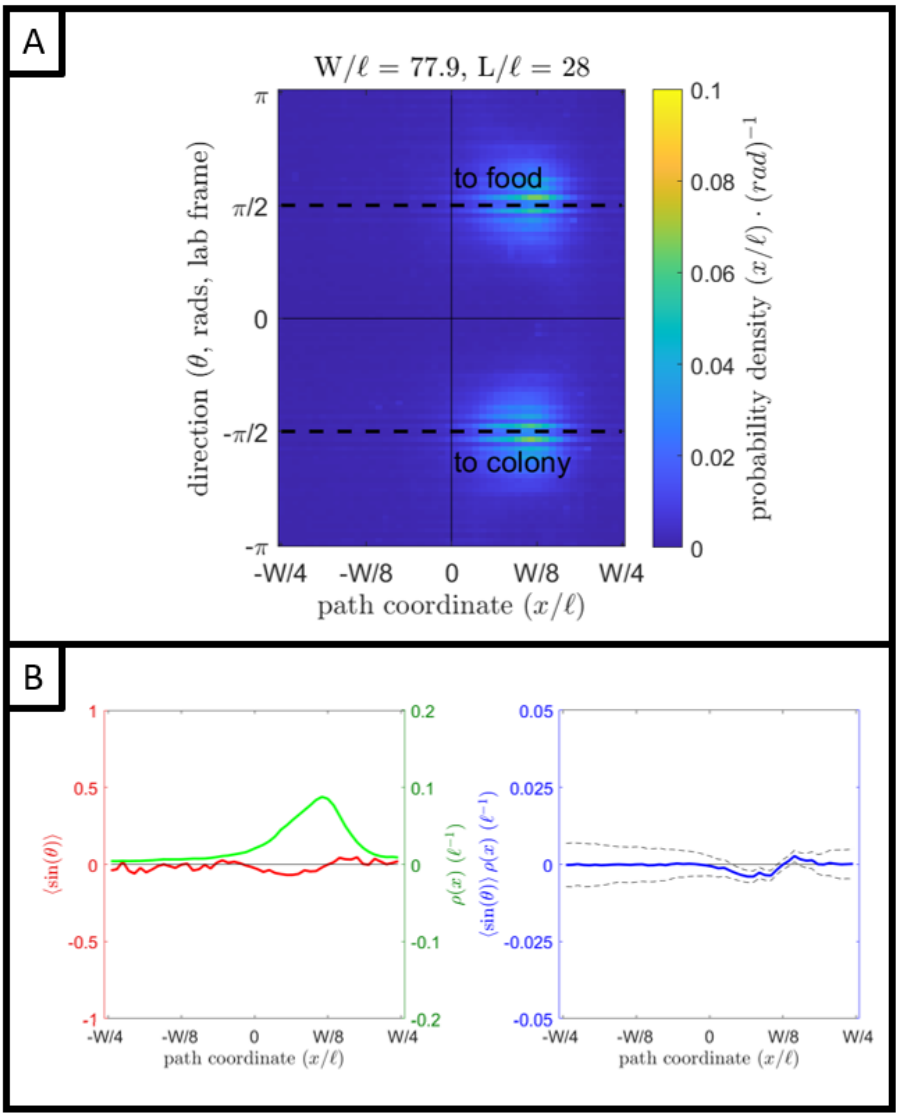

Figure 10. (A) Fundamental Laning Diagram, showing the angular density distribution as function of lateral position. W and L refer to the confining width and vertical imaging extent, respectively (B) Linear ant density (green) and net directionality (red) as function of lateral position. Their product, referred to as the flux correlate, is shown in blue. Error bars (dashed lines) are estimated from uncertainty in the net directionality and density, as well as the number of ants in the corresponding bin.

along the longitudinal direction. To fully explore the relationship between lateral position and lab-frame orientation, we can replace this vertical spatial axis with the lab frame angle θ, allowing us to organize the ants in 2D based on their positions and orientations (x_i, θ_i). If we bin the ants found near each position and angle (x, θ), we can measure the average density of ants per ant length per radian $(\frac{N}{(rad)(\ell)})$ in any particular frame. Figure 10A shows a heat map of this density field, with higher ant density represented by warmer colors. We refer to this plot as the fundamental laning diagram (FLD), as spatially and temporally persistent lanes which align with the food-nest axis result in localized peaks in both lateral position and angular density. Here, W refers to the lateral confining width, and L refers to the vertical extent of the observation region. For the unconfined *A.ceph* column, the FLD shows two regions of high ant density along the angular axis, one food-bound and one nest-bound ($\pi/2$ and $-\pi/2$ in the lab frame, respectively). These two angular peaks are nearly aligned along the lateral axis, emphasizing the bidirectional nature of the ants' transportation network. In this unconfined limit, the FLD does not reveal any obvious lane structures perpendicular to the direction of travel. This observation is reinforced by the 1D analysis presented in figure 10B, which shows the lateral density in green, lateral directionality in red, and corresponding flux correlate in blue. Error bars (dashed lines) are estimated from uncertainty in the net directionality and density, as well as the number of ants in the corresponding bin. Figure 11 shows the FCs and associated error bars for the same unconfined trials presented above. Due to the low density of *A.ceph* foragers and the high degree of mixed traffic in the unconfined limit, the estimates of the FCs' lateral dependence are statistically limited, with error bars which largely encompass the vertical axis and obscure any direct evidence of a

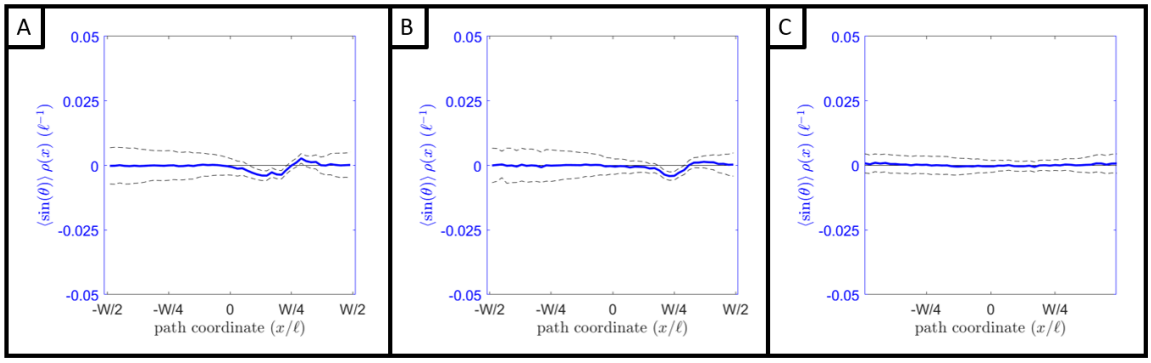

Figure 11. The lateral dependence of the flux correlate for the same three trials (A), (B), and (C) as above. Low ant density and large error bars in the unconfined limit prevent the direct observation of lane structures.

preferred flux orientation, especially in figure 11C. While some trials have regions do show preferred flux orientation, these structures are not consistent between trials.

2.5 Ant Frame Polar Density and Polar T-T Correlation

As previously described, the global structural output in an ant transportation network is an emergent property resulting from many individuals making decisions based on their unique local environments. Rather than analyze the dynamics of interactions on an individual level, we will instead attempt to characterize the perspective of the 'average' ant by calculating system properties like density and relative alignment in the reference frame of every individual (see figure 5B) and then averaging these results over all ants. We refer to these plots as 'perspective-based' or 'ant-frame', since the represent system parameters from the perspective of an average ant. Figure 12A shows the average perspective-based ant probability density in the unconfined foraging column averaged over all ants, and normalized over the circular region shown. For an ant located at $r = 0$ and oriented directly up the page, this plot shows the probability of finding a neighbor ant at each relative position and orientation (r, ϕ), with warmer colors indicating higher probability densities. The

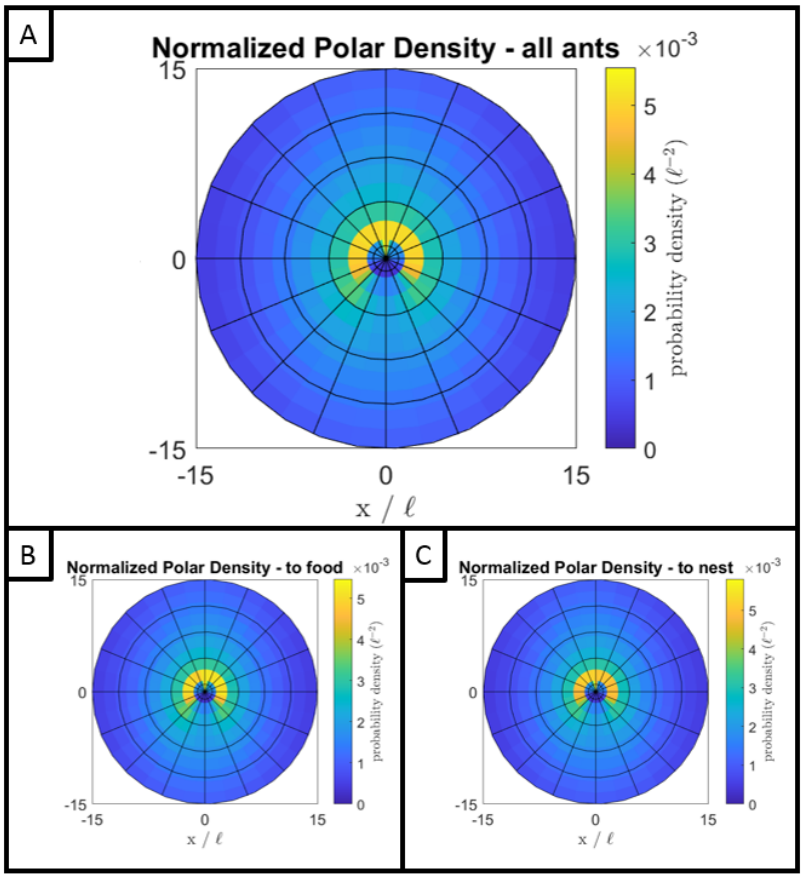

Figure 12. Ant Frame Polar Density. Heat map showing ant density ($\frac{n}{\ell^2}$) as a function of polar coordinates r and ϕ in the ant frame (see figure 5B). r is reported in ant lengths, and ϕ in radians. Polar density observed by (A) all, (B) nest-bound, and (C) food-bound ants

distribution reveals a peak neighbor density at a distance r between 1 and 3 ant lengths over a wide range of relative angles. The decrease in relative density at larger distances hints at the spatial inhomogeneity of ant density in the lab frame. If the ants spread uniformly through the observation region, there would be no decrease in ant density at higher distances from the average ant. Once again, the details of the ants' auto-chemotactic navigation result in specific signatures in our analysis. In addition to the radial density peak, figure 12A also shows a depletion zone directly to the rear of the average ant. This decreased ant density likely results from the preference for forward motion exhibited by individual ants, as the region directly

behind an ant in motion can only be immediately occupied by another ant moving in the same direction. In contrast, the region directly in front of any particular ant is not limited by prior occupation, and can be occupied by a forward or backward moving ant. This may result in the up-down asymmetry demonstrated in the polar density plot for all ants shown in figure 12A.

While useful for making observations about all actors in a foraging column, ant frame maps also allow us to explore how individual perspectives depend on their direction of travel. In figures 12B and 12C, we show the average perspective of ants who are food-bound and nest-bound respectively. As the three lane traffic pattern sometimes observed in ant foraging columns likely arises due to asymmetries in yielding between these groups [11], maps like these may provide insights into differences in decision making between the two classes, as demonstrated in other studies [15]. In the unconfined limit explored here, however, no obvious distinction can be drawn between these two groups of foragers. As the FC for these trials failed to reveal characteristics of a 3 lane structure, it is possible that some degree of confinement may be necessary for laning signatures to emerge in our analysis, with accompanying differences in these ant frame measurements.

In analogy with the lab frame measurements presented above, we can include orientation information in our ant frame measurements to explore the frequency of aligned and anti-aligned interactions as a function of distance and relative orientation from the average ant. As the orientation of each ant is given by the direction of its tangent vector, a good measure of relative alignment is the dot product between two unit vectors for a pair of ants, also known as the tangent-tangent (TT) correlation, equivalent to $cos(\theta_i - \theta_j)$ for lab frame orientations θ_i and θ_j. This measure varies from 1 to -1 for aligned and anti-aligned pairs, respectively. As with the density plots

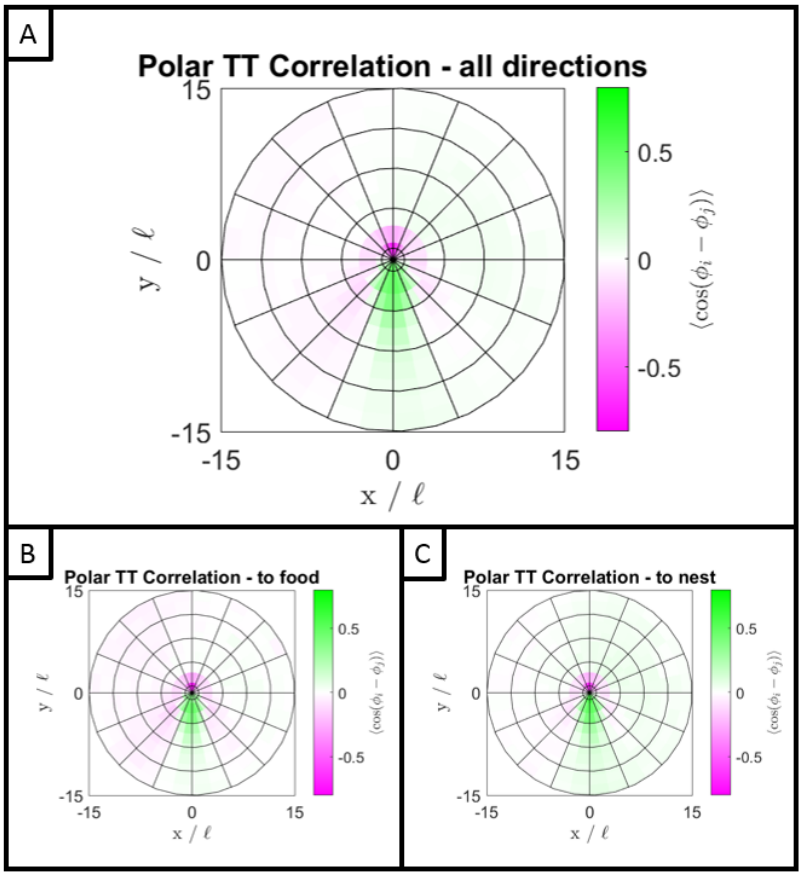

Figure 13. Ant Frame Tangent-Tangent Correlation, showing average relative orientation $< cos(\theta_i - \theta_j) >$ as a function of polar coordinates r and ϕ in the ant frame (see figure 5B). r is reported in ant lengths, and ϕ in radians, with the average ant oriented directly up the page. TT Correlation observed by (A) all, (B) nest-bound, and (C) food-bound ants

above, we calculate this observable in the reference frame of each ant, measuring the TT correlation between the central ant and every other individual in the frame at a particular r and ϕ before merging these observations into a single reference frame. We then spatially bin the TT values in r and ϕ and average them to explore the alignment field around the 'average' ant. We refer to the resulting plot as the polar TT correlation, shown in figure 13. When considering all ants as in figure 13A, we observe that individuals frequently experience alignment with neighbors behind them, while they are more likely to meet an anti-aligned partner directly in front of them.

These features can be explained by the ant's practice of 'antenating', or stopping to touch antennas [16]. The process can take less than a second, but this is enough to bias our sampled statistics in the fore region towards anti-alignment. Another feature of interest is the prominent anti-alignment behind and to either side of the average ant. Like water in front of a boat, antenating ants disengage and pass on either side while maintaining their proximity, resulting in the observed anti-alignment profile referred to as a 'wake'. For the trial shown, these anti-aligned regions are slightly asymmetric, suggesting the ants in our system show a slight preference for passing opposing traffic on the right. As with the density plots above, we can group individuals based on their global orientation to explore the differences in alignment observed by food-bound and nest-bound ants, as shown in figures 13B and 13C. While the wake described above is present from the perspective of both classes, food-bound ants experience a higher degree of anti-alignment in their immediate vicinity compared with nest-bound ants in the same observation region. This observation is in agreement with the observed tendency for unladen, food-bound ants to yield preferentially to nest-bound traffic [11], resulting in a lower frequency of head-to-head collisions and a reduced wake for laden ants.

In addition to these proximal differences, we can also observe a large scale right-left asymmetry in the relative orientation of more distant ants. Figure 13A suggests an overall preference for alignment on the right and anti-alignment on the left. This trend can also be seen in the conditional plots in figure 13B and 13C as well. While this asymmetry does not seem to result in any obvious organization in the lateral flux distribution, it is possible that under sufficient confinement this statistical tendency may result in the sudden emergence of an asymmetric lane structure, highlighting the potential for dynamic phase transitions to occur in active matter systems.

2.6 Conclusion

By characterizing the statistical properties of this foraging column in the unconfined limit, we measured the natural width of the ant path, as well as the details of its lateral flux distribution in the steady state. While we can easily extract measures of mean position and lateral spread from this data set, the low ant density and minimal directional segregation across the lateral extent of the path limits the amount of information we can extract about the columns organization of flux. Despite this limitation, observations reported in the ant frame show organizational signatures that we speculate result from nematic alignment, spatial localization, antenating, and a preference for forward motion. This underscores the value of these perspective based plots for studying interactions between individuals, as well as the behavioral characteristics of the average ant, even when lab frame measurements do not show strong evidence of spatial structure. With the results shown in this chapter, we are now prepared to study the structure and dynamic evolution of the foraging column under different levels of lateral confinement.

CHAPTER III

THE DYNAMICS OF PATH STRUCTURE AND ORGANIZATION UNDER CYCLIC CONFINEMENT

We now explore how the ant transportation network responds to changes in lateral confinement by restricting the *A.ceph* foragers to a 2D plane of variable width. In order to explore extreme levels of confinement for long periods without severely limiting the colonies caloric intake, we cyclically compress and expand the confining barriers and collect data under 10 different conditions: 5 widths under expansion, and 5 under compression to complete a single cycle. This cycle is repeated 5 times with the resulting ant observations grouped by condition before analysis. We present the results of this experimental procedure from two separate width ranges. In both regimes, physical barriers produced regions in the observation window with an average ant density of zero. To ease visual comparison between these different widths, we normalize the lateral representation of the data based on confinement level and report all positions in ant lengths.

3.1 Moderate Confinement

3.1.1 Structure in the Lab Frame

Our results in section 2.2 suggest that the unconfined path has a natural width of $W_{path} \approx 2\sigma_x \approx 13.4$ ant lengths, approximately 5.1 cm. Our first investigation into the statistical properties of the confined path explore it's properties under moderate confinement, here defined as confining widths from approximately 1.0 $W_{conf.}$ to 0.5 $W_{conf.}$, a range of 5.0 to 2.5 cm. Figure 14 shows a sample of 6 width-normalized FLDs averaged over 5 compression-expansion cycles under moderate width restriction. These plots reveal that the foraging column experiences peak ant density when maximally confined. As the foragers travel at approximately constant speeds and

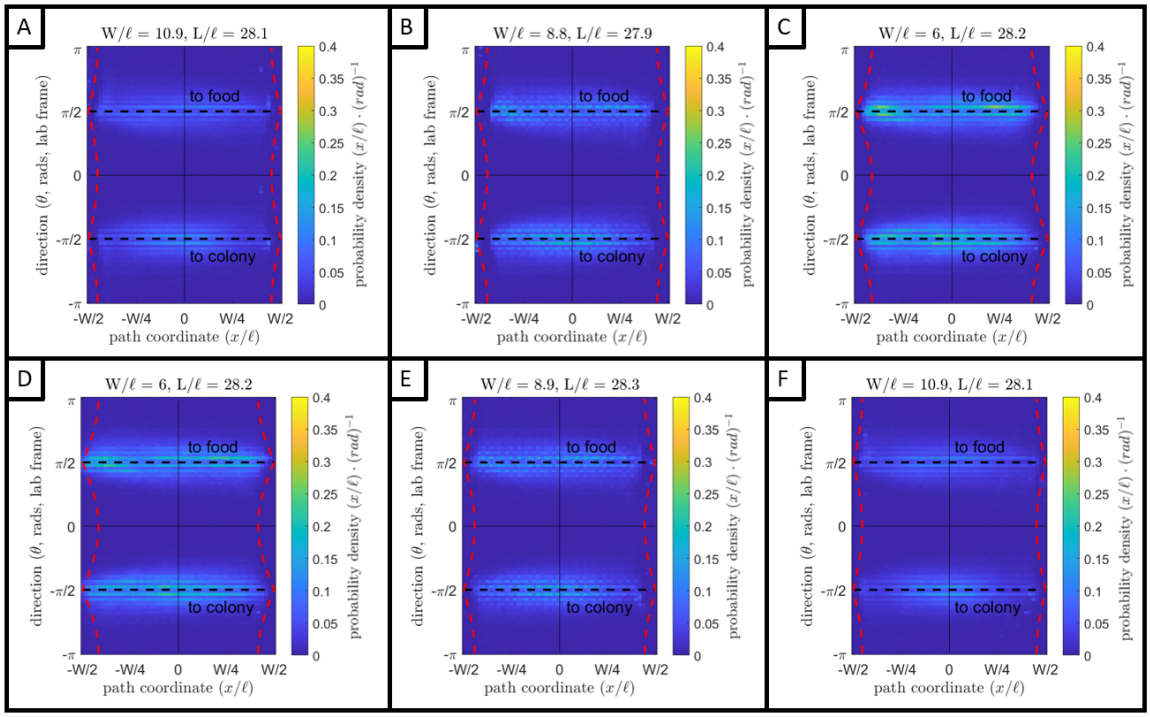

Figure 14. FLD as function of width, moderate confinement. (A) 5.0 cm, (B) 3.3 cm, (C) 2.5 cm, all during compression. (D) 2.5 cm, (E) 3.3 cm, (F) 5.0 cm, all during expansion. The width and length of the confining region are provided for each plot in units of average ant length. Red dashed lines enclose regions of ant-wall exclusion.

must collectively maintain some baseline level of caloric input, the survival of the colony depends on the *A.ceph*'s ability to maintain different densities under different degrees of lateral restriction. At high density, the energetic cost of individual collisions can be mitigated by improving the lateral organization of ant flux through the creation of lanes. Examples of this increased organization can be found in Fig 14C and 14D, where ant traffic centered around the food-bound direction $\pi/2$ nucleates into two distinct spatial peaks, and traffic centered around the nest-bound direction $-\pi/2$ becomes more concentrated near the path center. This trend suggests that the *Atta cephalotes* (*A.ceph*) engage in a statistical three lane traffic pattern under moderate confinement, where the outer sides of the path are preferentially occupied by food-bound ants, with a central lane dominated by nest-bound individuals.

At these widths, steric interactions between the ants and move-able barriers can create exclusion zones whose properties depend on the positions and orientations of the barriers, as well as the instantaneous confining width. Figure 15 shows a schematic representation of this steric exclusion process, highlighting combinations of positions and orientations which are allowed and disallowed due to ant-wall interaction in green and red, respectively.

To verify that the organizational changes observed in Fig 14 are not a consequence of these exclusion zones, and instead arise from behavioral shifts in the ant population, we calculate the minimum distance to the wall the average ant can attain based on their vector orientation (see chapter 4.1) and record these values. We then plot this minimum displacement vertically on the FLD as a function of orientation. In figure 14, this minimum displacement is indicated for both walls with red dashed lines. These curves allow us to enclose the geometrically excluded regions on the FLD and compare the predicted depletion with that in the observational data. Under moderate confinement (2.5 – 5.0 cm) these marked regions closely align with boundary of the ant density profile, especially for ants closely aligned with $\pm\frac{\pi}{2}$. Conveniently, the

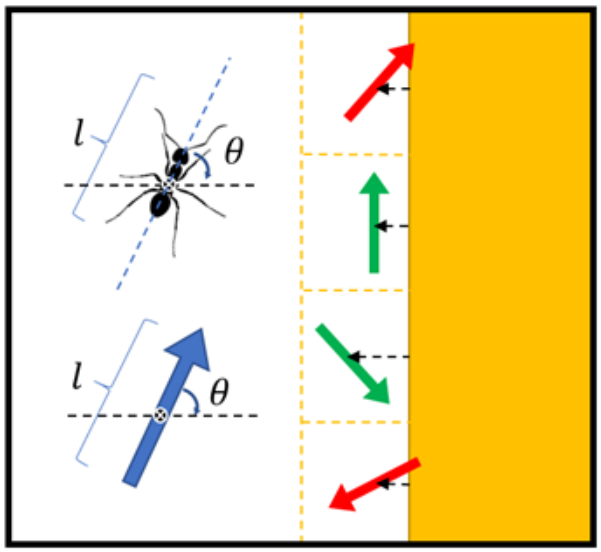

Figure 15. Geometric modeling of ant-wall steric exclusion. In the lab frame, ants can be represented as vectors with lengths and orientations. Certain orientations and distances from the confining wall are excluded by steric interactions (red) while others are not (green). Minimum allowed ant-wall distance depends on the projection of any *A.ceph* vector onto the lateral axis.

high degree of nematic alignment exhibited by the *A.ceph* in this system keeps most individuals near these orientations, where the width of the excluded region goes to 0, having a minimal impact on the lateral density profile. For ants oriented far from the food-nest axis, the depletion in the density profile becomes spatially asymmetric, showing a larger exclusion zone than predicted by the static geometric theory for some combinations of position of orientation. This additional depletion can be observed on the left side or the right side of the path for lab frame orientations of $\theta = 0$ or $\pm\pi$ respectively, resulting in an 's' shaped density profile. This shape likely arises from a combination of the ant's preference for forward motion and their limited turn radius [17], since some combinations of orientation and ant-wall distance would require individuals to 'back-up' to the confining walls. Further theoretical modeling is required to fully include this observed trend in our hypothesized exclusion zones, and fitting these parameters in future investigations may provide insight into system parameters like minimum turn radius and average ant velocity.

To best characterize the lateral flux distribution as a function of width, figure 16 shows the width normalized FC for the same 6 trials presented in figure 14. The large uncertainty near the right and left edges of these plots result from the decrease in ant density closest to the confining walls. In this representation, the three lane traffic pattern is readily apparent at all confinement levels, with regions of flux which are definitively positive or negative, even with the inclusion of estimated uncertainty. This analysis also allows us to explore any differences in system behavior due to direction of barrier motion, a property referred to as hysteresis. At this level of confinement, neither the FLDs nor the FCs show any significant structural hysteresis due to direction of barrier motion, although the overall ant flux is slightly lower during expansion compared to compression. In contrast with the unconfined path,

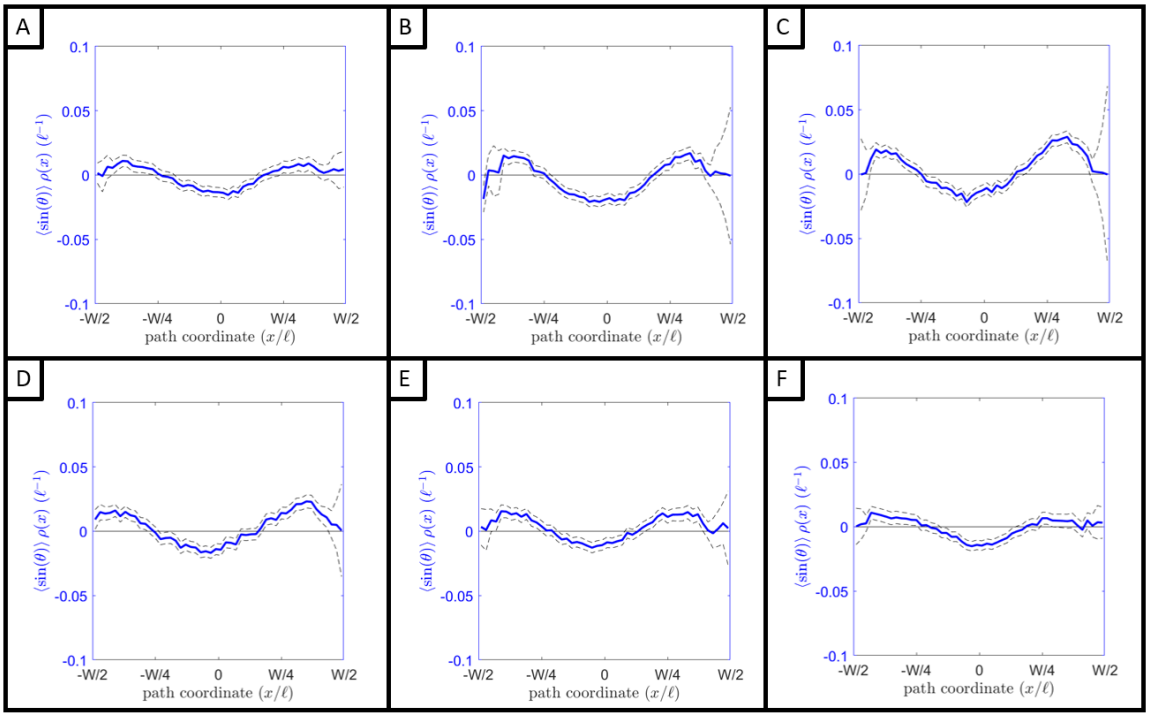

Figure 16. Flux Correlate as function of width, moderate confinement. (A) 5.0 cm, (B) 3.3 cm, (C) 2.5 cm, all during compression. (D) 2.5 cm, (E) 3.3 cm, (F) 5.0 cm, all during expansion. Black dashed lines show error bars calculated from the number of ants associated with each data point and the corresponding uncertainty on density and average orientation. The flux correlate shows a 3 lane pattern at all widths, with maximum flux shown at the highest confinement level (C, D).

a foraging column under moderate confinement shows a dramatic increase in lateral organization, as seen in the lab frame.

3.1.2 Structure in the Ant Frame

We now implement the perspective based analysis techniques presented in section 2.5 to explore how the perspective of the average ant depends on the instantaneous confinement level. Figure 17 shows the polar density plots corresponding to the same confining widths presented in figure 14. In contrast with the unconfined path represented in section 2.5, here the radial distance to the peak density shows a strong dependence on the relative angle; when looking to the left or right, the average ant sees a dramatic drop-off in neighbor density compared to the vertical, aligned axis.

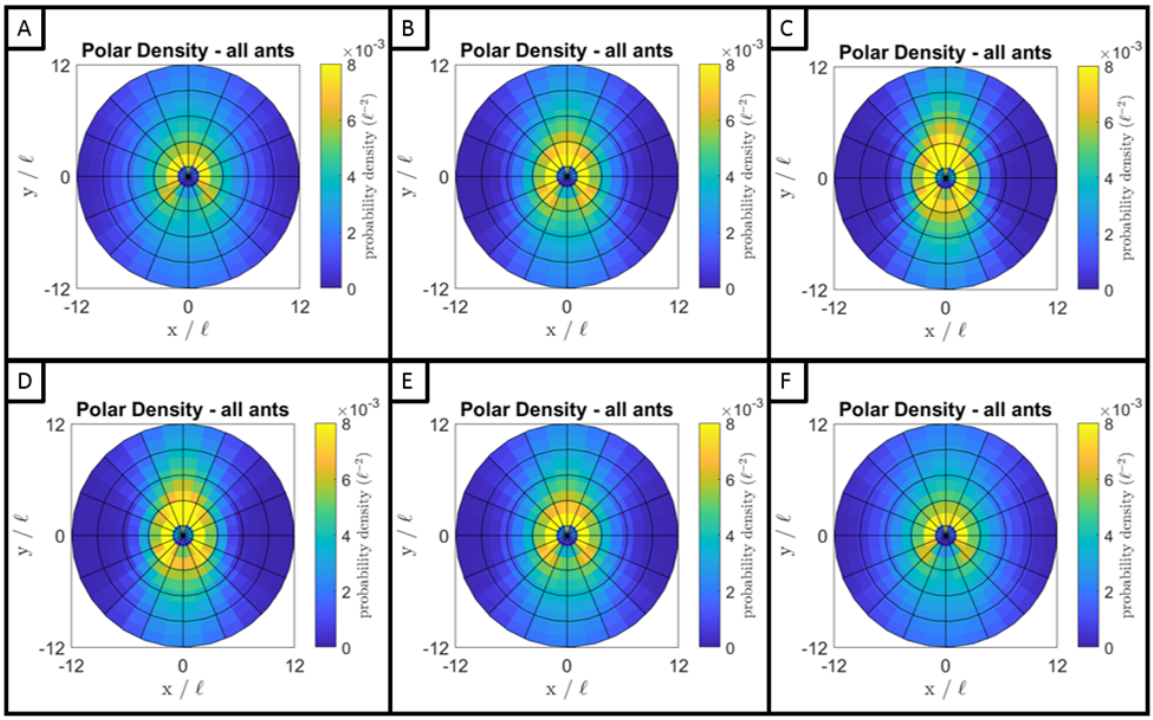

Figure 17. Perspective-based Polar Density as a Function of Width, moderate confinement. (A) 5.0 cm, (B) 3.3 cm, (C) 2.5 cm, all during compression. (D) 2.5 cm, (E) 3.3 cm, (F) 5.0 cm, all during expansion.

At the higher levels of confinement represented in fig 12C and 12D, this drop-off is even more pronounced. This change in the density profile results from a combination of steric confinement and the ant's nematic alignment along the food nest axis. If the ants were just as likely to be found oriented perpendicular to the path as along it, then half of the sampled regions of steric depletion would fall in front of and behind individual ants, resulting again in a radial density profile with no dependence on relative direction. As emphasized in the FLDs presented in figure 14, the ants' tendency to nematically align with the food-nest axis results in the observed depletion zones.

While the wake observed in the unconfined limit is still present under this degree of confinement, at the narrower widths represented by figures 17C and 17D the front-

back asymmetry described in 2.5 becomes less pronounced. This suggests that under higher confinement levels, the statistical tendency for ants to engage in head on collisions may be reduced by an increased degree of laning, balancing the ant density found in front-of and behind the average ant, resulting in a higher degree of front-back symmetry in plots of polar density.

Figures 18 and 19 present the ant-frame density plots for nest-bound and food-bound ants respectively. Even at this confinement level, there is still no strong distinction between the relative density observed by the two groups. These conditional plots show similar degrees of width dependent asymmetry as that shown when considering all ants. While not observed here, higher degrees of confinement may cause orientation-dependent behavioral changes in the confined ants, resulting in visible differences in this perspective based representation.

As first exemplified in the unconfined limit, we now include orientation information in our perspective based to plots to study how the alignment field around the average ant responds to changing confinement levels. The Polar TT correlation introduced in section 2.5 is shown in figure 20 for the same trial and confinement levels as above. These plots allow us to explore how the degree of relative alignment experienced by the average ant in our system depends on the degree of steric confinement.

In agreement with the TT Correlation for the unconfined foraging column (see figure 13), at these widths the previously described front-back asymmetry and anti-aligned wake are both present in the confined column over the full range of lateral compression. These plots also reveal a slight right-left asymmetry, with the same preference shown for passing oncoming traffic on the right. The persistence of this asymmetry over such a wide range of width restriction suggests that at sufficient

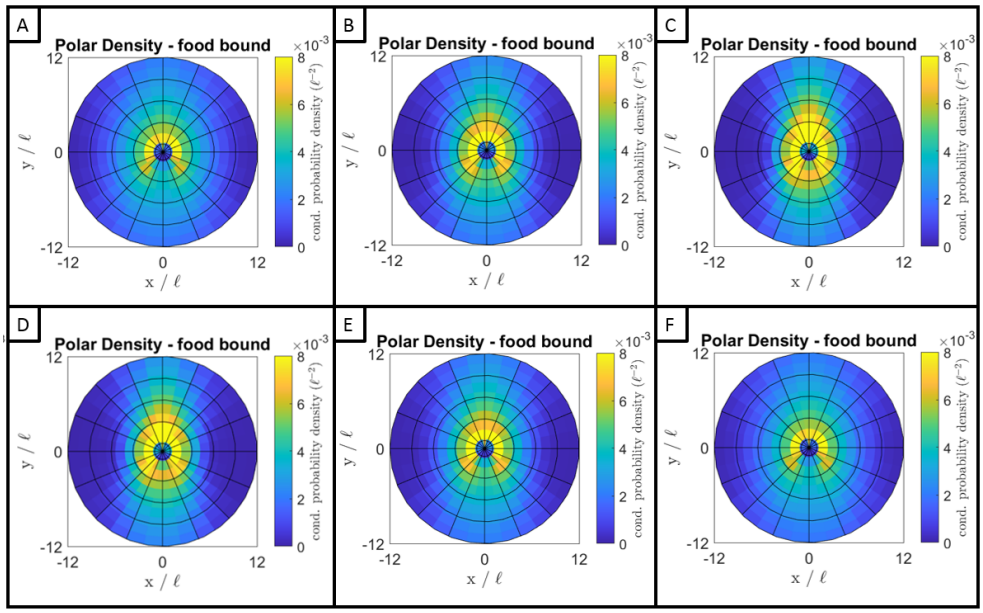

Figure 18. Perspective-based Polar Density as a Function of Width, moderate confinement, nest-bound. (A) 5.0 cm, (B) 3.3 cm, (C) 2.5 cm, all during compression. (D) 2.5 cm, (E) 3.3 cm, (F) 5.0 cm, all during expansion.

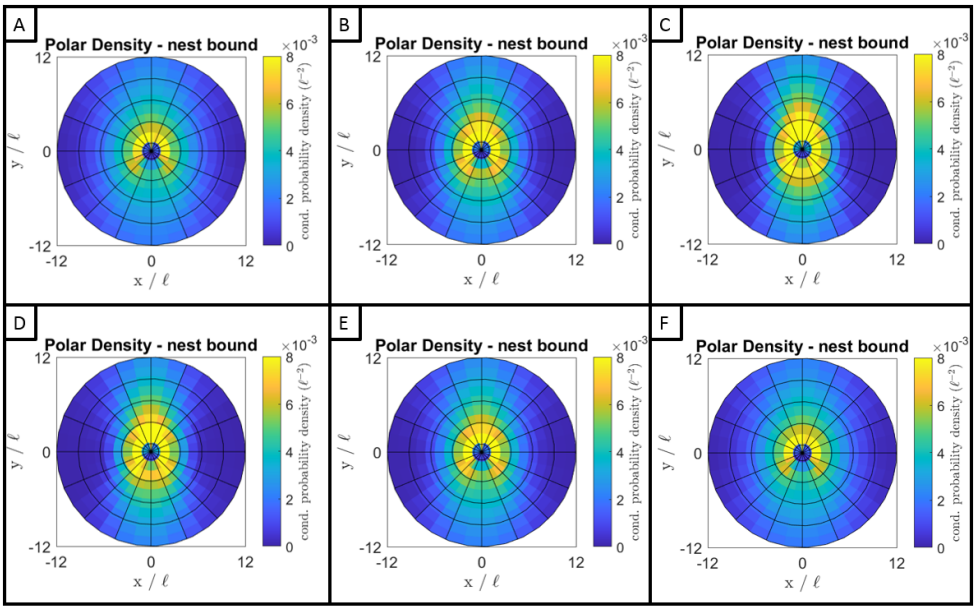

Figure 19. Perspective-based Polar Density as a Function of Width, moderate confinement, food-bound. (A) 5.0 cm, (B) 3.3 cm, (C) 2.5 cm, all during compression. (D) 2.5 cm, (E) 3.3 cm, (F) 5.0 cm, all during expansion.

confinement, there will be a statistical preference for one organizational chirality, resulting in a discernible 2 lane traffic pattern.

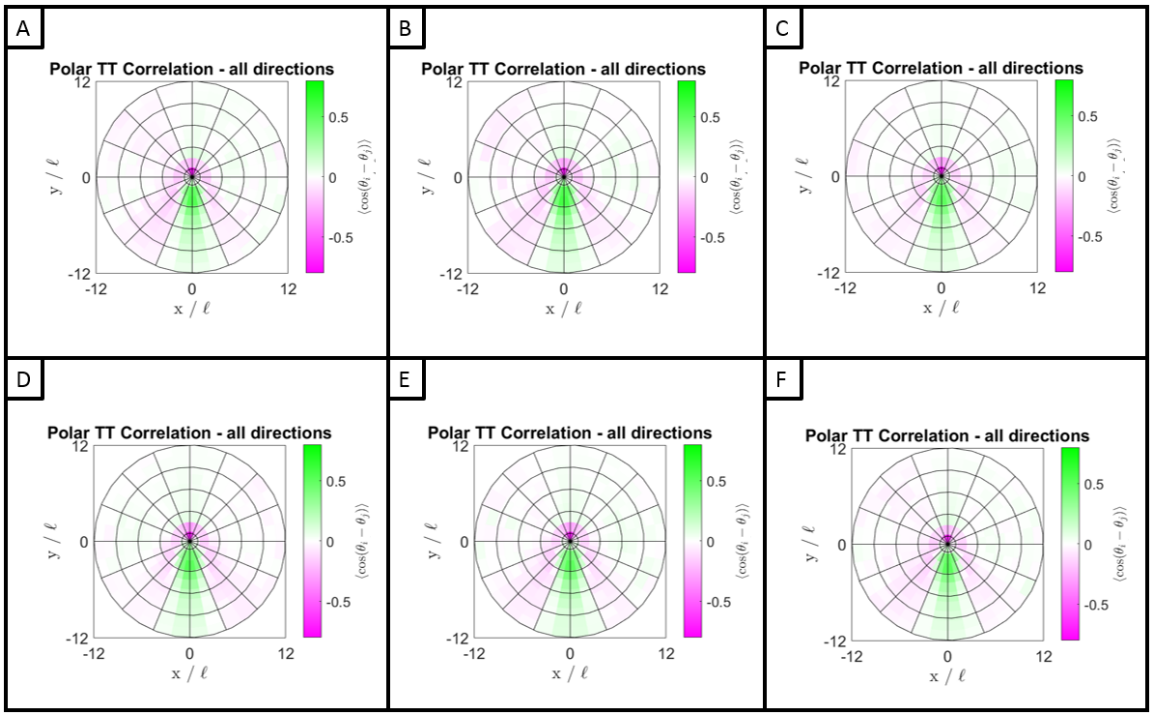

Figure 20. Perspective-based TT Correlation as a Function of Width, moderate confinement, all ants. (A) 5.0 cm, (B) 3.3 cm, (C) 2.5 cm, all during compression. (D) 2.5 cm, (E) 3.3 cm, (F) 5.0 cm, all during expansion.

In contrast with the polar density plots, the inclusion of orientation information provides some evidence for hysteresis between compression and expansion in the ant column, especially when the ants are grouped by their direction of travel. When comparing the plots in figure 21B and 21E for all ants, there is a discernible depletion in anti-alignment on the right side present under expansion, resulting in higher degree of right-left asymmetry than that shown under compression. Of the two groupings represented in figure 21 and 22, this trend is strongly mirrored by the food-bound individuals, while the TT Correlation for nest-bound ants shows no strong changes in right-left symmetry at any confinement level. This observation suggests that food bound ants react more strongly to environmental changes. As the 3 lane traffic pattern shown for *Atta cephalotes* likely results from an higher level of spatial reactivity in food

bound ants, the distinct asymmetry shown in these perspective-based plots reinforces the potential for directionally dependent behavior among the *A.ceph* foragers.

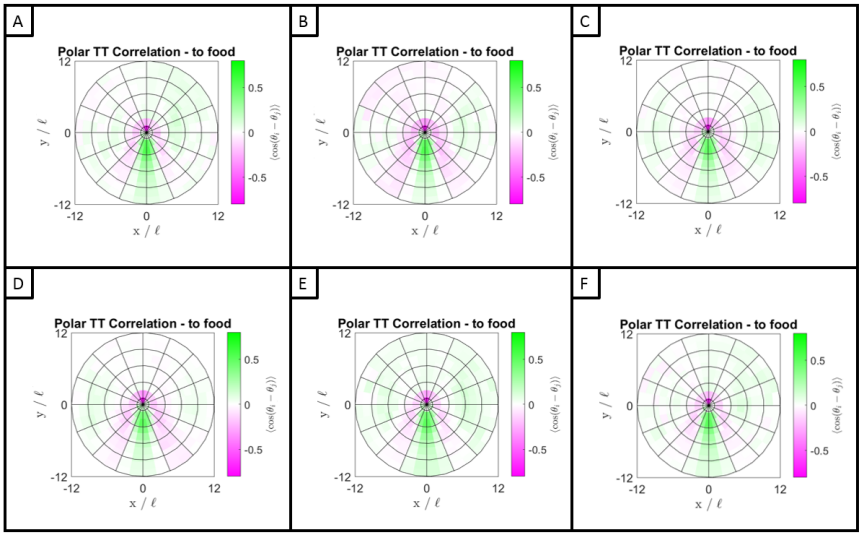

Figure 21. Perspective-based TT Correlation as a Function of Width, moderate confinement, food-bound. (A) 5.0 cm, (B) 3.3 cm, (C) 2.5 cm, all during compression. (D) 2.5 cm, (E) 3.3 cm, (F) 5.0 cm, all during expansion.

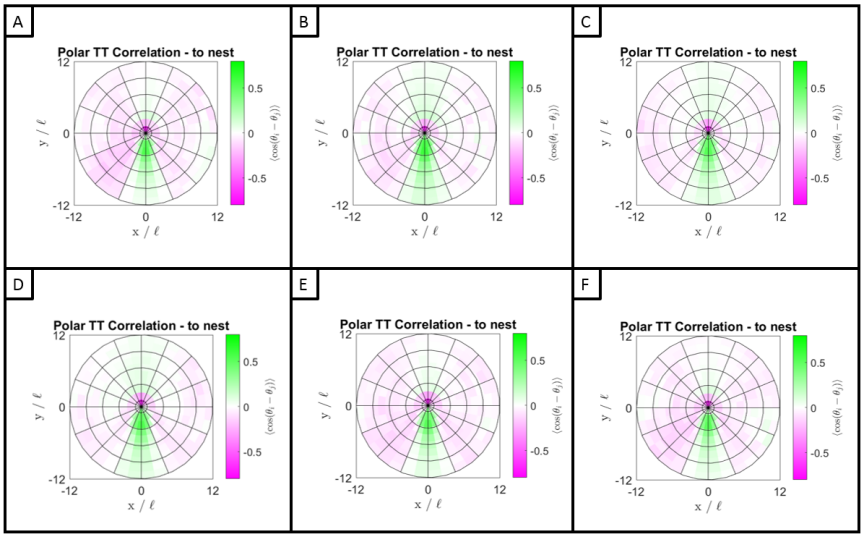

Figure 22. Perspective-based TT Correlation as a Function of Width, moderate confinement, nest-bound. (A) 5.0 cm, (B) 3.3 cm, (C) 2.5 cm, all during compression. (D) 2.5 cm, (E) 3.3 cm, (F) 5.0 cm, all during expansion.

3.2 Extreme Confinement

After quantifying the organizational characteristics of the path near its natural width, we continue our investigation into the dynamic evolution of these structures for widths much smaller than that imposed by the ants' auto-chemotaxis. Here, extreme confinement is defined as confining widths from approximately 0.7 W_{path} to 0.2 W_{path}, a range of 3.5 to 1.0 cm. As the average ant length in our system is approximately $\ell = 3.8$ mm, the maximum confinement level explored in experiment is less than 3ℓ, and likely below the minimum width required to maintain a steady 3-lane traffic pattern. Such a narrow path will likely prompt significant changes in the organizational structure when compared with the results under moderate confinement.

3.2.1 Structure in the Lab Frame

To accommodate the vertical extent of the foragers leaf fragments, the moveable walls separating the floor and ceiling of the of the observation region have a height of 2.5 cm. To restrict foragers to the 2D plane below, we apply talc to these vertical surfaces before each experiment, but over the long integration times (6 days) employed in these experiments, persistent attempts at climbing by the ants can eventually remove the talc layer and provide alternative, out-of-plane paths. As our current ant identification model can not discriminate between ants on the barriers and ants on the observation platform, our presented results include the statistics of these wall climbing individuals, especially at the minimum path width.

Figure 23 shows the FLD as a function of the provided lateral width restriction. At these widths, a distinct aliasing pattern results from a mismatch in resolution between the neural net's localization and the histogram bin size. Under compression and expansion, a dramatic change in the lateral distribution of both nest-bound and

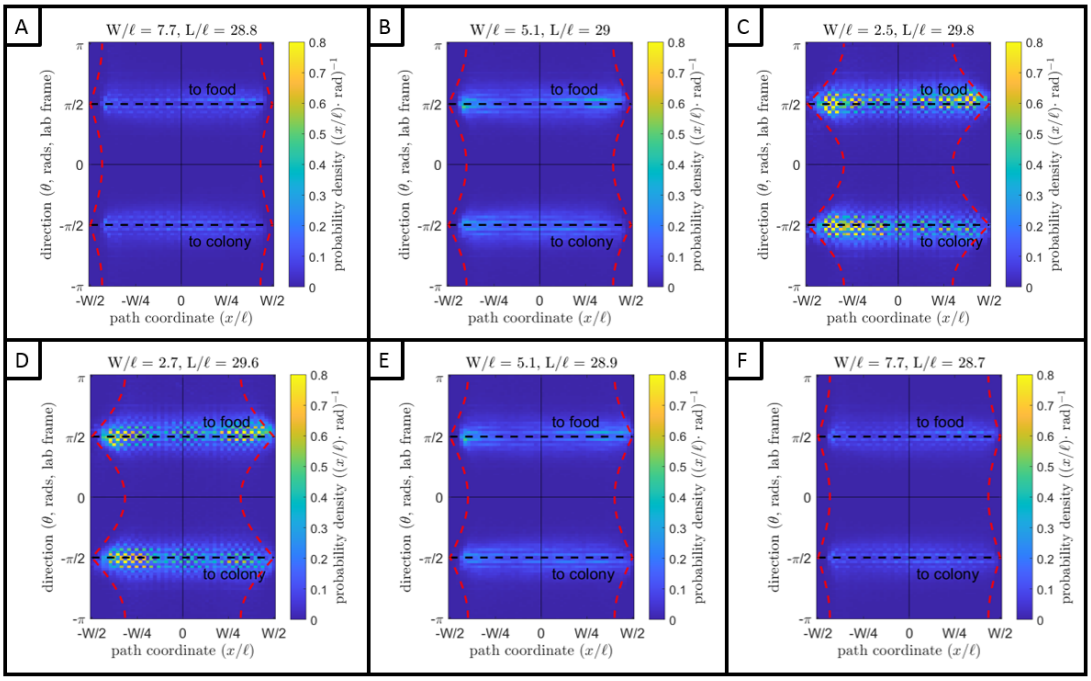

Figure 23. FLD as function of width, extreme confinement. (A) 2.5 cm, (B) 1.8 cm, (C) 1.0 cm, all during compression. (D) 1.0 cm, (E) 1.8 cm, (F) 2.5 cm, all during expansion. The width and length of the confining region are provided for each plot in units of average ant length. Red dashed lines enclose regions of ant-wall exclusion.

food-bound ants can be observed between the widths of 5.1ℓ and 2.5ℓ. At a path width of 2.5 ant lengths, food-bound ants are still likely to be found on either side of the path, though with a slightly narrower spatial profile on the left side of the plot. In contrast, nest-bound ants show a shift from a peak in density near the path center to a strongly asymmetric density profile. If restricted to a 2D surface, this density distribution would result in a high rate of head to head collisions and an overall reduced foraging efficiency. Rather, the changes in the food-bound distribution show the effects of ants not restricted to the plane. Viewed from below, these ants all appear at the same x position, concentrating the density distribution on the side of the path shown in figure 23, and producing the sharp spike seen in the width dependent FC in figure 24 for the same trial.

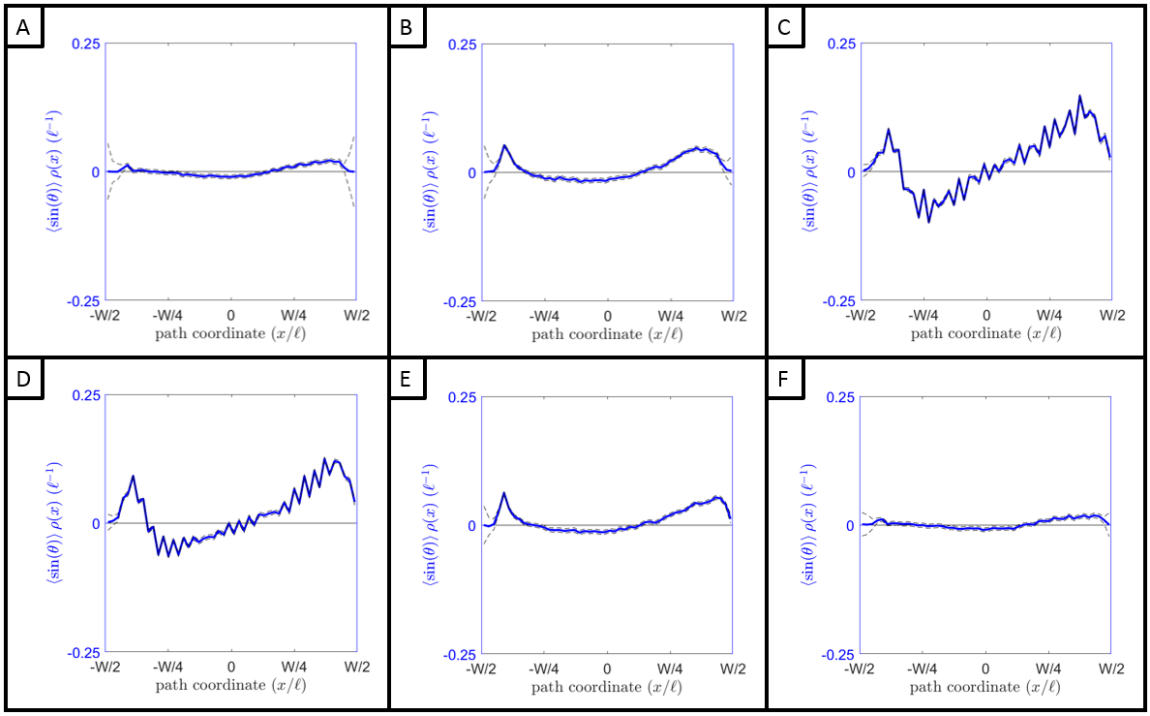

Figure 24. FC as function of width: Extreme Confinement. (A) 2.5 cm, (B) 1.8 cm, (C) 1.0 cm, all during compression. (D) 1.0 cm, (E) 1.8 cm, (F) 2.5 cm, all during expansion.

The side of the path impacted by out-of-plane ants appears to be consistent across the 5 trials integrated for this analysis. While this consistency may represent a quantifiable preference for wall climbing on one side of the path, it may also result from a stochastic process in the first compression-expansion cycle, with climbing in consecutive trials influenced by which side of the path has a modified talc barrier, in a simple example of energy minimization. Travel along a vertical surface has a higher metabolic cost, explaining why the number of wall climbers and the corresponding sharpness of the left-most peak in the FC change so dramatically over such a small change in width. As maintaining the 3 lane traffic pattern shown at lower confinement levels becomes increasingly difficult, it eventually outweighs the inefficiencies associated with travel along a vertical surface. When the column is allowed to expand, many of these wall climbers return to the observation platform.

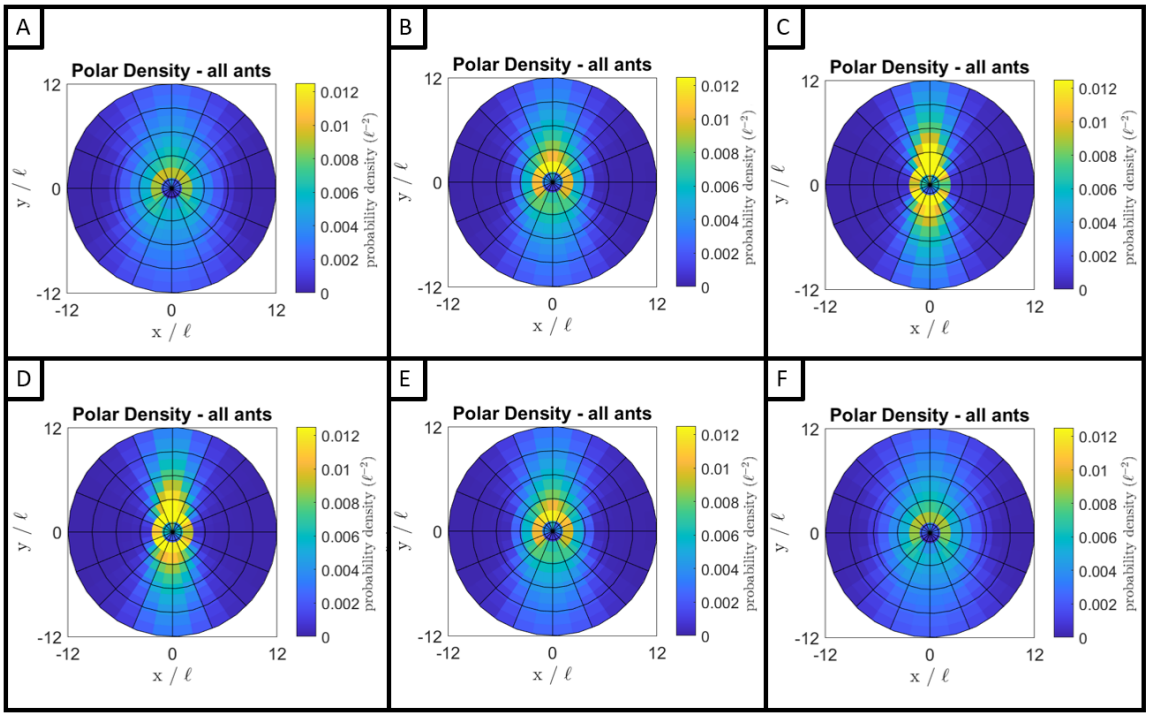

Figure 25. Perspective-based Polar Density as a Function of Width: Extreme Confinement, all ants (A) 2.5 cm, (B) 1.8 cm, (C) 1.0 cm, all during compression. (D) 1.0 cm, (E) 1.8 cm, (F) 2.5 cm, all during expansion.

This width dependent behavioral switch is reproducible in our system, highlighting additional ways in which the foraging column can optimize its opposing flux.

3.2.2 Structure in the Ant Frame

In that ant frame, we first present the width dependent polar density in figure 25. for the extremely confined path. Once again, the lateral width restriction coupled with the average nematic alignment results in a higher pair density in front of and behind the average ant in the system. In addition, the previously described wake disappears at peak confinement, in agreement with the results from the moderately confined path.

As before, we separate the ants into groups depending on their global orientation to distinguish between the polar densities observed by individuals traveling in different

directions. Figure 26 shows the polar density from the perspective of the food-bound ants, while figure 27 shows it from that of the nest-bound ants. There is a slight distinction between the angular distribution of ant density at the narrowest width; nest-bound ants observe an angled density profile with respect to their heading. As the ants returning to the colony show the largest degree of spatial asymmetry in lab frame density, we anticipate the emergence of these asymmetric features in their perspective based plots as well, even if influenced by the inclusion of out-of-plane ants.

Finally, we present the total agent-based TT Correlation for *Atta cephalotes* under extreme confinement, as well as the same plots for individuals grouped by global orientation in figures 28, 29 and 30.

In agreement with the TT Correlation for the unconfined foraging column (see figure 13), at these widths the front-back asymmetry and anti-aligned wake are both present in the confined column over the full range of lateral compression. These plots also reveal a right-left asymmetry which may result from the out-of-plane individuals. This possibility is reinforced by the results in figures 29 and 30, which show the same plot for ants separated by global orientation. While unique width-dependent asymmetries are present for both groups, extracting rules for interaction from these plots will require alternative containment methods to prevent out-of-plane individuals from influencing the interpretations.

3.3 Conclusion

Under confinement, the behavior of the *A.ceph* foragers results in an obvious traffic pattern and corresponding flux organization with a direct dependence on the imposed width. Under moderate confinement near the natural path width, the

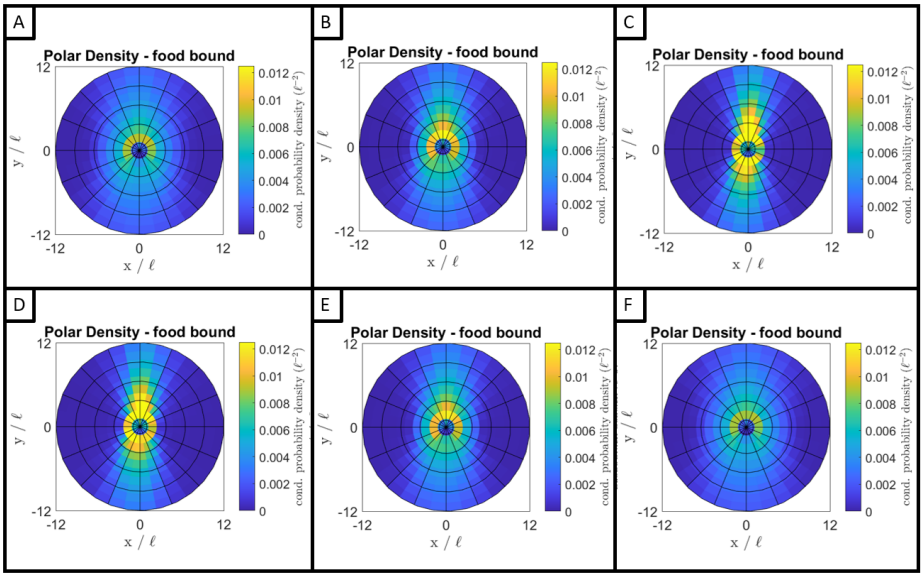

Figure 26. Perspective-based Polar Density as a Function of Width: Extreme Confinement, food-bound. (A) 2.5 cm, (B) 1.8 cm, (C) 1.0 cm, all during compression. (D) 1.0 cm, (E) 1.8 cm, (F) 2.5 cm, all during expansion.

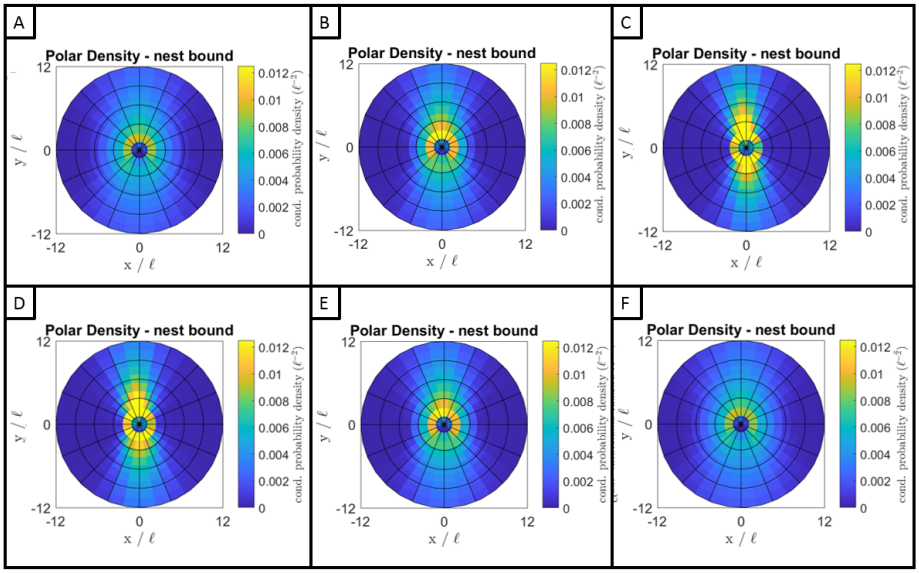

Figure 27. Perspective-based Polar Density as a Function of Width: Extreme Confinement, nest-bound. (A) 2.5 cm, (B) 1.8 cm, (C) 1.0 cm, all during compression. (D) 1.0 cm, (E) 1.8 cm, (F) 2.5 cm, all during expansion.

results presented above suggest that *Atta cephalotes* engage in the same 3 lane traffic previously identified in other species, especially *Eciton burchelli* and *Atta colombica*. The higher ant density exhibited by the *A.ceph* under this confinement gives our FC

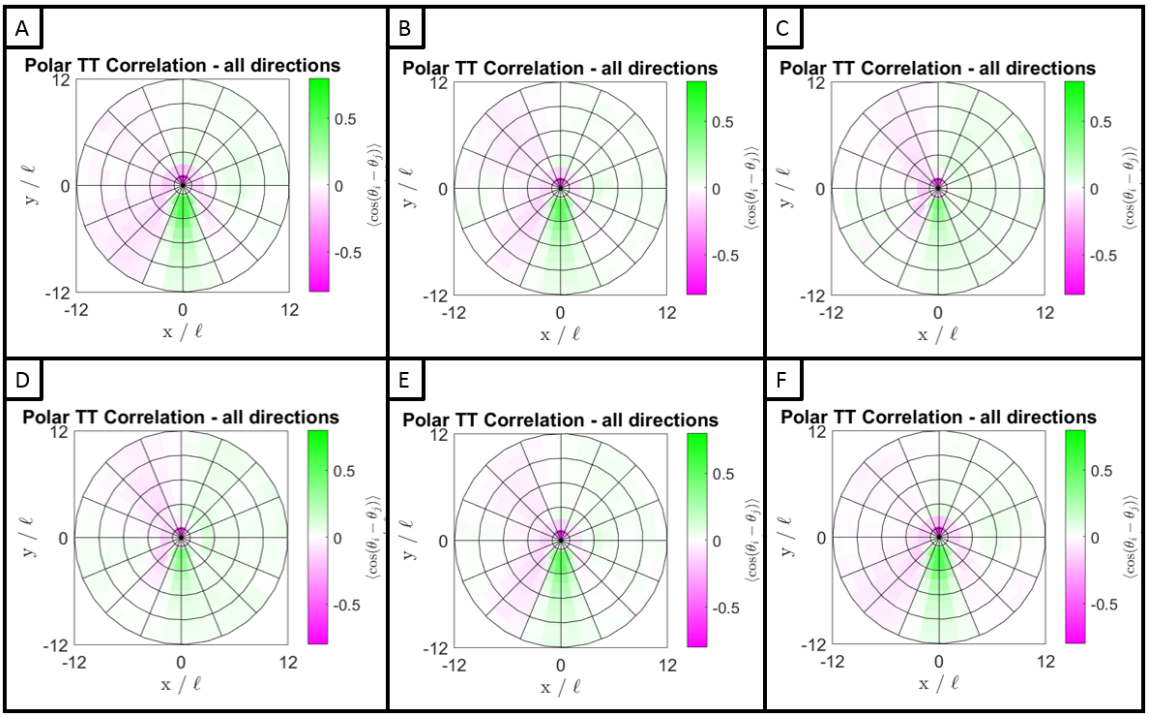

Figure 28. Perspective-based TT Correlation as a Function of Width, extreme confinement, all ants. (A) 2.5 cm, (B) 1.8 cm, (C) 1.0 cm, all during compression. (D) 1.0 cm, (E) 1.8 cm, (F) 2.5 cm, all during expansion.

plots the statistical significance necessary to claim the definitive observation of lane structures. In the ant frame, the effects of steric confinement can be easily observed in plots of polar density, while the TT correlation emphasizes behavioral changes under different widths for both nest-bound and food-bound individuals. These plots provide an avenue for understanding how the behavior and spatial perspective of the average individual react to dynamic environments.

Under extreme confinement, the *A.ceph* demonstrate a simple form of energetic minimization by utilizing metabolically expensive vertical pathways only when the cost of maintaining the steady-state 3 lane pattern becomes prohibitive due to the level of confinement. This analysis suggests the critical width for the observed transition is between 1.8 and 1.0 cm, or 5.1 and 2.5 ℓ. In order to identify a similar

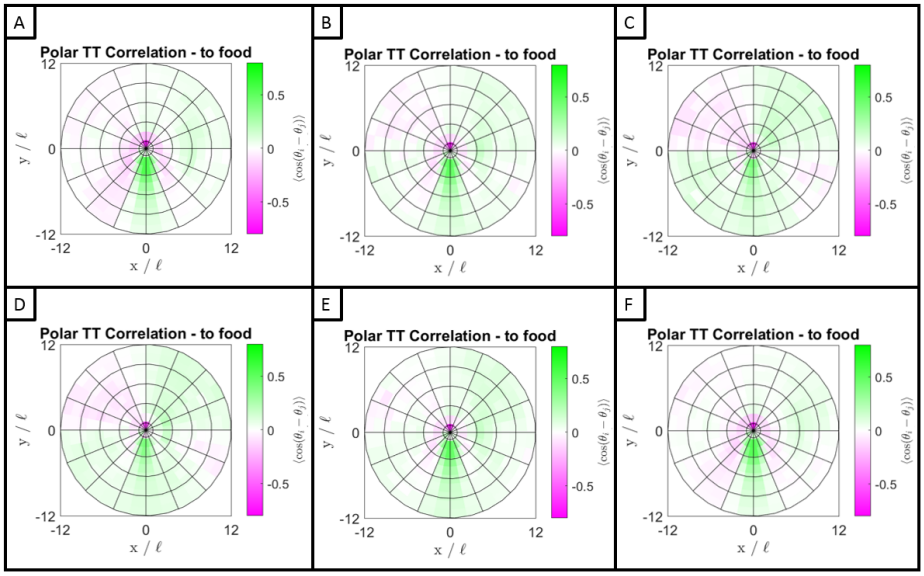

Figure 29. Perspective-based TT Correlation as a Function of Width, extreme confinement, food-bound. (A) 2.5 cm, (B) 1.8 cm, (C) 1.0 cm, all during compression. (D) 1.0 cm, (E) 1.8 cm, (F) 2.5 cm, all during expansion.

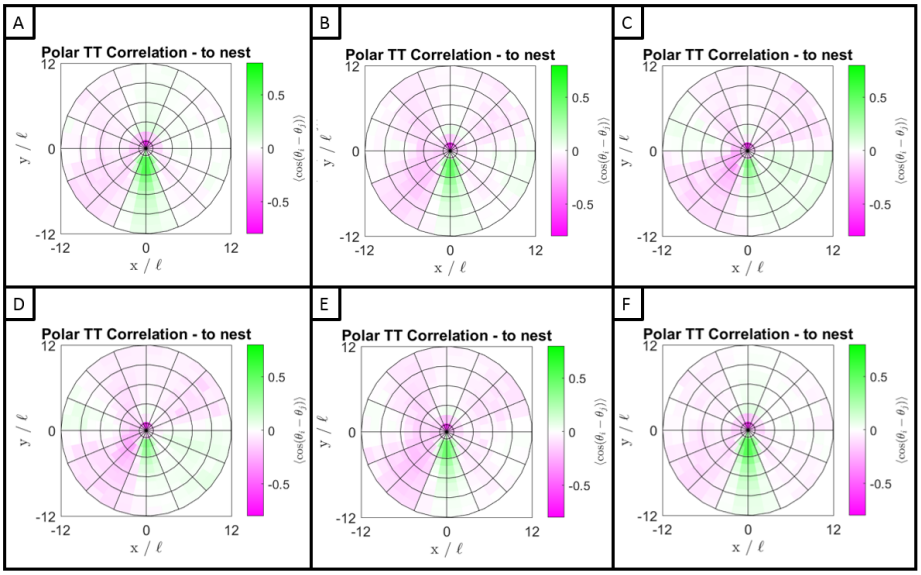

Figure 30. Perspective-based TT Correlation as a Function of Width, extreme confinement, nest-bound. (A) 2.5 cm, (B) 1.8 cm, (C) 1.0 cm, all during compression. (D) 1.0 cm, (E) 1.8 cm, (F) 2.5 cm, all during expansion.

transition point between a 3 and 2 laned path structure, alternative containment methods will be necessary to better restrict the *A.ceph* to the 2D plane, or similar

analyses may be carried out on an ant species not dependent on a vertical clearance like the leaf-cutters studied here.

While the analysis of our experimental data shows structures and trends which support our understanding of ant behavior, it may be necessary to observe the same outcomes for data which is completely unstructured. As a comparison, we now prepare to explore the simplest model of *A.ceph* behavior, where structures and trends result only from steric interactions, and not from behavioral changes in the ants.

CHAPTER IV

COMPARING EXPERIMENTAL OBSERVATIONS TO THE 'NULL' MODEL OF *ATTA CEPHALOTES* TRANSPORTATION

4.1 The 'Null' Model of *A.ceph* Behavior

While the data presented so far has aimed to showcase the organizational properties of the ant path, for both lab frame measurements and ant frame maps the structure in these plots results from a combination of steric constraints in the system, and the decision making of individual ants. To reliably extract information about this decision making, we first need to understand what portion of the structure in these plots comes from sterics alone. We achieve this by generating an artificial data set under the assumption that average lab frame density is a constant, while the frame-by-frame ant number number follows a Poisson Distribution with a fixed mean number of ants. The position and orientation for each ant is chosen at 'random', assumed initially to be uniform in both x, y, and θ, but restricted by the three basic processes of occlusion: image bounds, ant-wall interactions, and ant-ant interactions. In simulating the positions and orientations of the *A.ceph*, we restrict the foragers to the same vertical extent as that sampled by our imaging system. Ant-wall occlusion, first described in chapter 2 and presented schematically in figure 15, treats the *A.ceph* foragers as orientable vectors in the lab frame. For ants of a given length ℓ, with a lab frame orientation of θ, we model the minimum lateral distance d_{lat} an in-plane ant must maintain from a nest-food aligned barrier as

$$d_{lat}(\theta) = \frac{\ell}{2} cos(\theta)$$

Conditional expressions in our simulation implement these two physical restrictions on simulated ants before adding them to the data set. Finally, we prevent

ant-ant occlusion during the placement process by checking for overlap between the line segment representations of the placed individual and those already in the frame. If any ants overlap, all of the intersecting individuals are removed from the frame. At very high confinement levels or extremely high densities this placement technique can cause a dramatic drop off in total ant count. Since this effect only occurs as a consequence of overlapping ant vectors, physical restrictions prevent *A.ceph* from maintaining densities which would cause such dramatic percolation in simulation. Overall, including the effects of ant-ant steric exclusion in our simulation results in a slightly lower average ant number in each frame.

4.2 Null Statistics in the Unconfined Limit

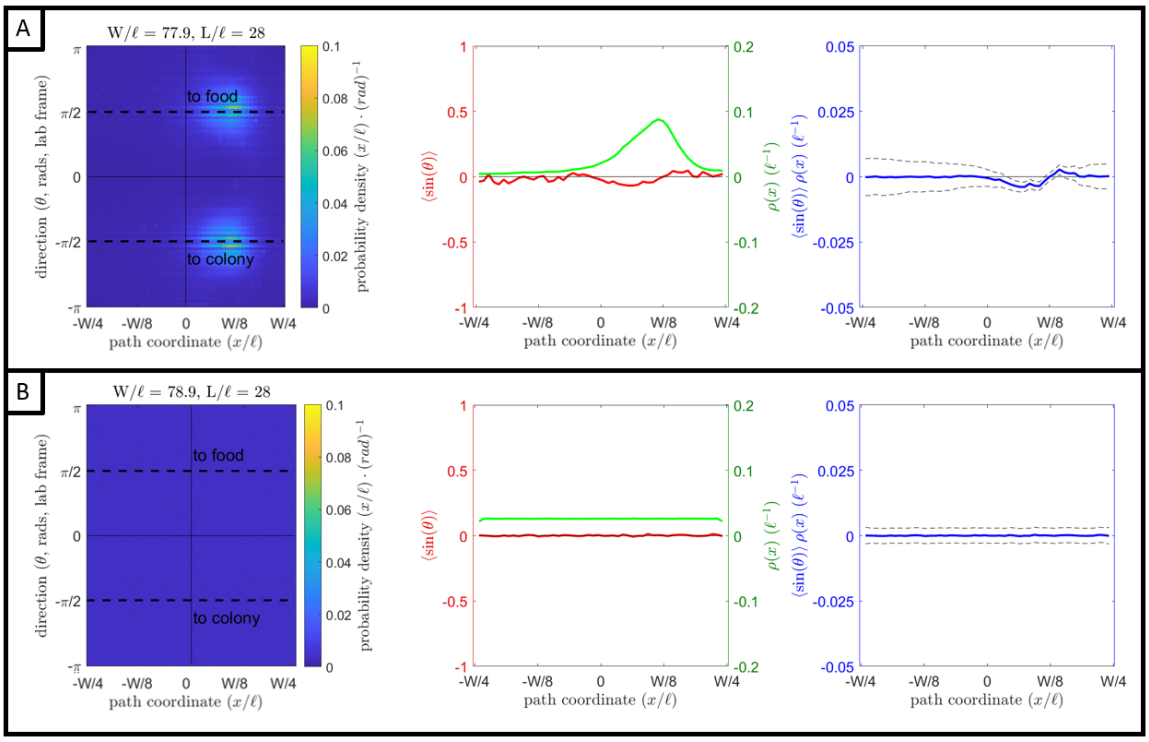

Figure 31. Laning in the Null Model (A) FLD and FC for the *A.ceph* foragers in the unconfined limit (B) FLD and FC from simulated ants under the same steric confinements.

We first explore the results of this null simulation for the unconfined foraging column. Figure 31 compares the results presented in chapter 2 for the FLD, lateral

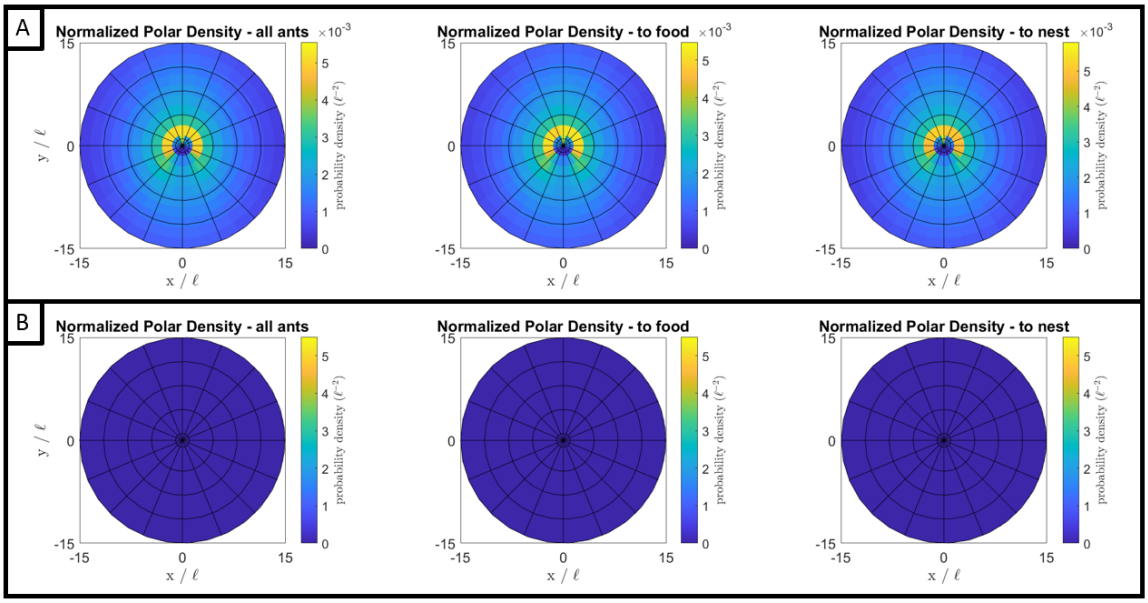

Figure 32. Polar density in the null model (A) Plots of polar density in the ant frame for the *A.ceph* foragers in the unconfined limit (B) Polar density of simulated ants under the same steric confinement. Both (A) and (B) show all ants, food-bound ants, and nest-bound ants from left to right.

density and directionality, and corresponding FC with those predicted by the null model of *A.ceph* behavior. In 31B, both appear completely flat, in alignment with uniform sampling in both position and orientation used to generate the simulated distribution. This comparison emphasizes the amount of organizational structure present in the foraging column, especially along the orientation axis.

We also compare the ant frame polar density and TT correlation in figures. 32 and 33. The polar plots show a dramatic difference between the perspective-based ant densities, as the auto-chemotactic navigation strategy represented by figure 32A results in a peak local ant density which exceeds that of null prediction by an order of magnitude. This observation holds when averaging over all ants or when grouping by orientation.

For the TT Correlation, the results of the null simulation shown in figure 33B contain a distinct lack of structure in the relative orientation of ants, especially when

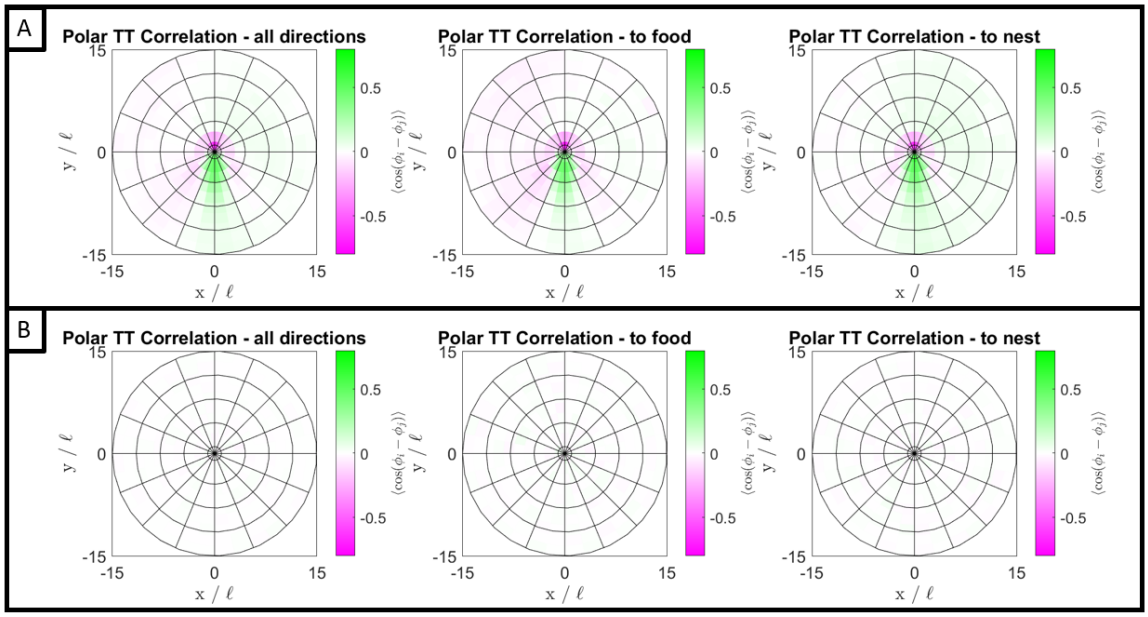

Figure 33. Polar TT correlation in the null model (A) Plots of the TT Correlation in the ant frame for the *A.ceph* foragers in the unconfined limit (B) FLD and FC from simulated ants under the same steric confinement. Both (A) and (B) show all ants, food-bound ants, and nest-bound ants from left to right.

directly compared with the same plots for the *A.ceph* foragers. This contrast serves to emphasize the large amount of structural information which can be extracted from this observable, potentially providing insights into the interaction rules and behavioral rules employed by the *A.ceph* foragers.

4.3 Null Statistics under Moderate and Extreme Confinement

We continue our investigation into the null hypothesis by implementing the same simulation and analysis techniques under varying levels of steric confinement. For this section, we compare these results to those produced by the *A.ceph* under three distinct widths, all representing behavior under compression (increasing confinement). While we do not show results for expansion, the lack of structural hysteresis demonstrated in chapter 3.1.1 suggests that our system operates near the adiabatic limit, with results largely independent of the direction of barrier travel.

In figure 34, The FLDs for the null model and the collected data are presented side by side for 3 confinement levels. For the simulated data, the effects of ant-wall exclusion are apparent, with a high degree of correlation between the edge of the depletion zone and its theoretical boundary. Without the internal behavioral rule-sets present in the *A.ceph*, ants in the null model fully sample the available space, yielding an FLD more sensitive to the degree of confinement at orientations far from the nest-food axis. Aside from overall density increase at smaller widths, the lack of structural change in these lab-frame plots further reinforces how the organization exhibited by the true foragers results from individual behavior, and not from system sterics. While not shown here, the FCs corresponding to these FLDs show the same lack of organization, suggesting a net flux of zero at all lateral positions across the path.

Figures 35 and 36 compare the ant frame measurements of polar density and TT correlation between the simulated and collected data over the same 3 widths as above.

Under extreme confinement, the comparisons are equally dramatic. Figure 37 gives the FLD, polar density, and TT correlation for the highest confinement level explored in this study for both the observational data and the null simulation. While largely in agreement with the moderately confined column, at the minimum width the spatial regions impacted by ant wall sterics begin to dominate the statistics of ant distribution, limiting the spread of individual orientation in the lab frame, and causing a slight directional dependence on the radial distribution of ant density observed by the average ant in our system, as shown in figure 37B. Despite this steric structuring present in ant frame measurements, the polar density shown by the *A.ceph*

foragers still reveals organization far beyond that imposed by ant wall interactions, and continues to emphasize the role of behavior in the results presented in chapter 3.

4.4 Conclusion

Primarily, this chapter serves to contrast the complexity of behavior exhibited by the *Atta cephalotes* foragers with the simplest, null model of behavior where individuals simply diffuse through the observation region. Through this method, we can emphasize the degree of nematic alignment present in our foraging column, and showcase its consequences in both the lab frame and the ant frame. We also highlight the emergence of lanes, and show by comparison that the laning signatures described in this study do not emerge as a consequence of ant-wall interactions, but from individual decision making. As described in chapter 3, the models implemented here for ant-wall exclusion do not consider the forward motion and limited turn radius of individual ants when predicting depletion zones. Increasing the complexity of our model from these simplest assumptions will allow us to better fit these depletion zones, and continue to zoom in on how individual decision making directly influences the global organization and structure of the foraging column.

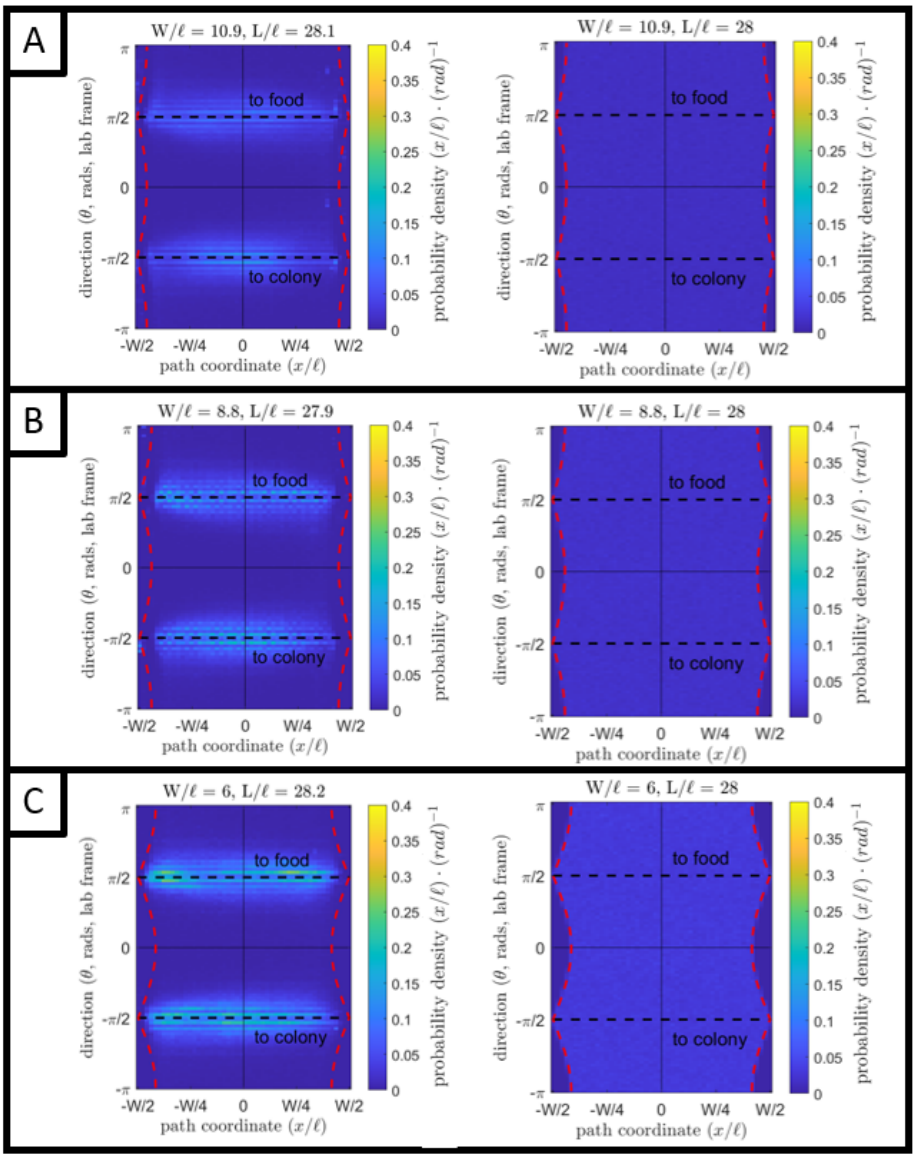

Figure 34. FLDs under the null model, moderate confinement. Comparisons shown between data and simulation (left and right, respectively) for confining widths of (A) 5cm, (B) 3.8 cm, and (C) 2.5 cm

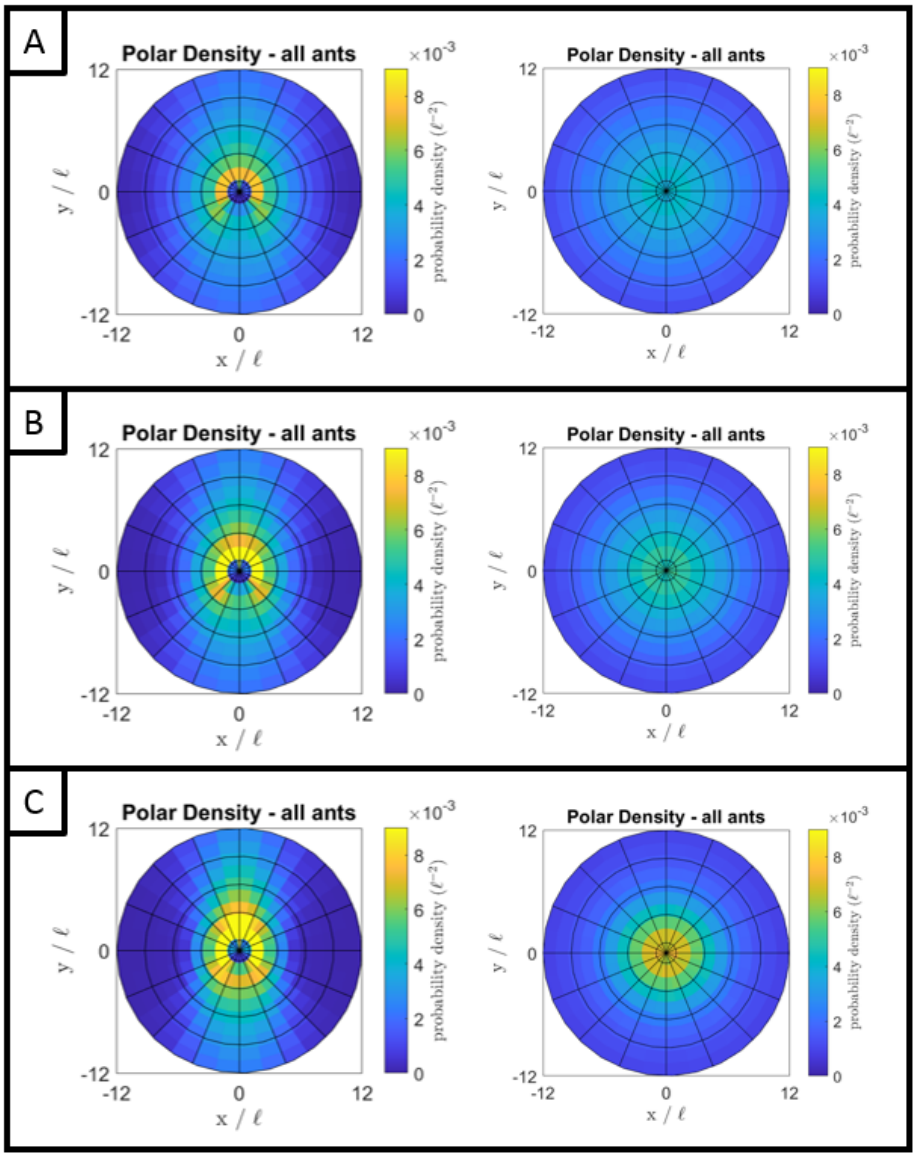

Figure 35. Ant frame polar density under the null model, moderate confinement. Comparisons shown between data and simulation (left and right, respectively) for confining widths of (A) 5cm, (B) 3.8 cm, and (C) 2.5 cm

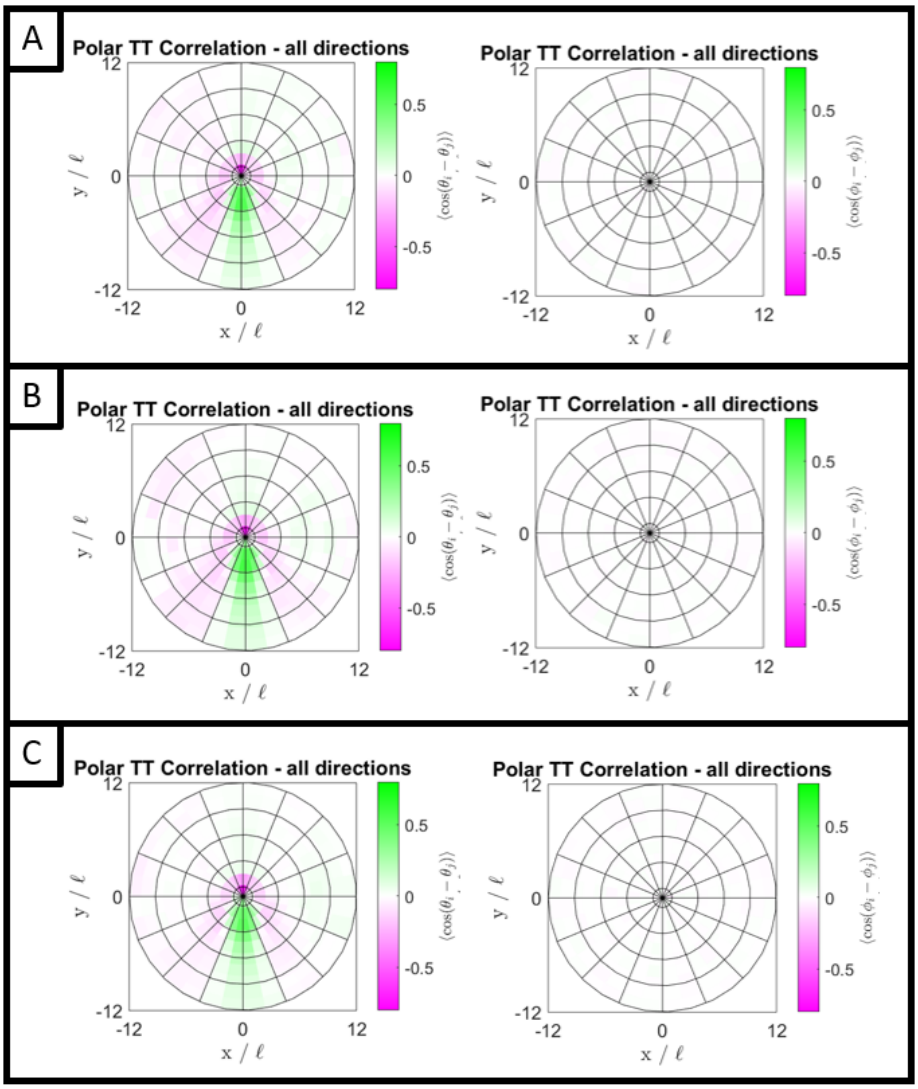

Figure 36. Polar TT correlation under the null model, moderate confinement. Comparisons shown between data and simulation (left and right, respectively) for confining widths of (A) 5cm, (B) 3.8 cm, and (C) 2.5 cm

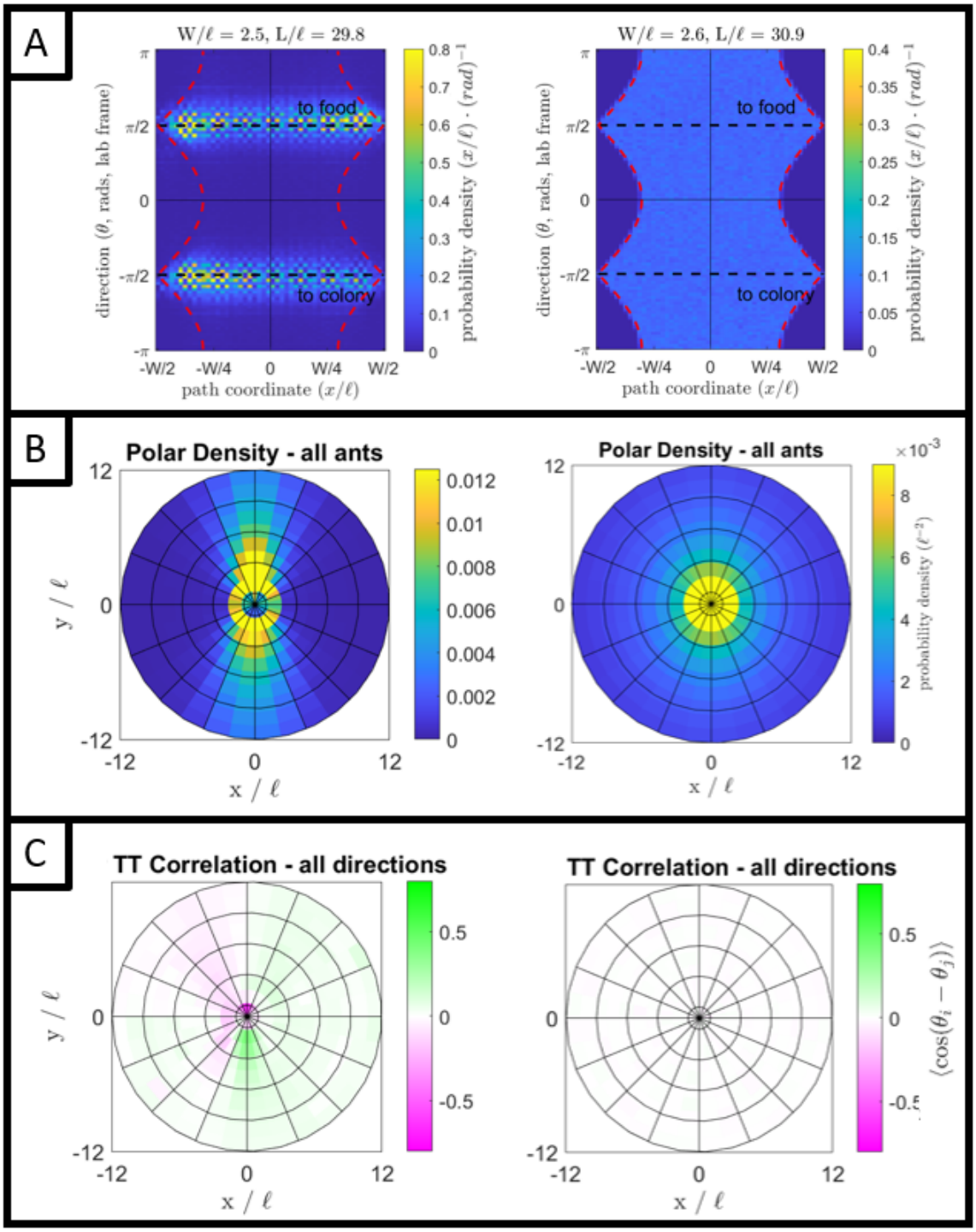

Figure 37. (A) FLD, (B) Polar density, and (C) TT correlation under maximum confinement (1 cm). Comparisons shown between data and simulation (left and right, respectively)

CHAPTER V

MATERIALS AND METHODS

5.1 Ant Colony Maintenance

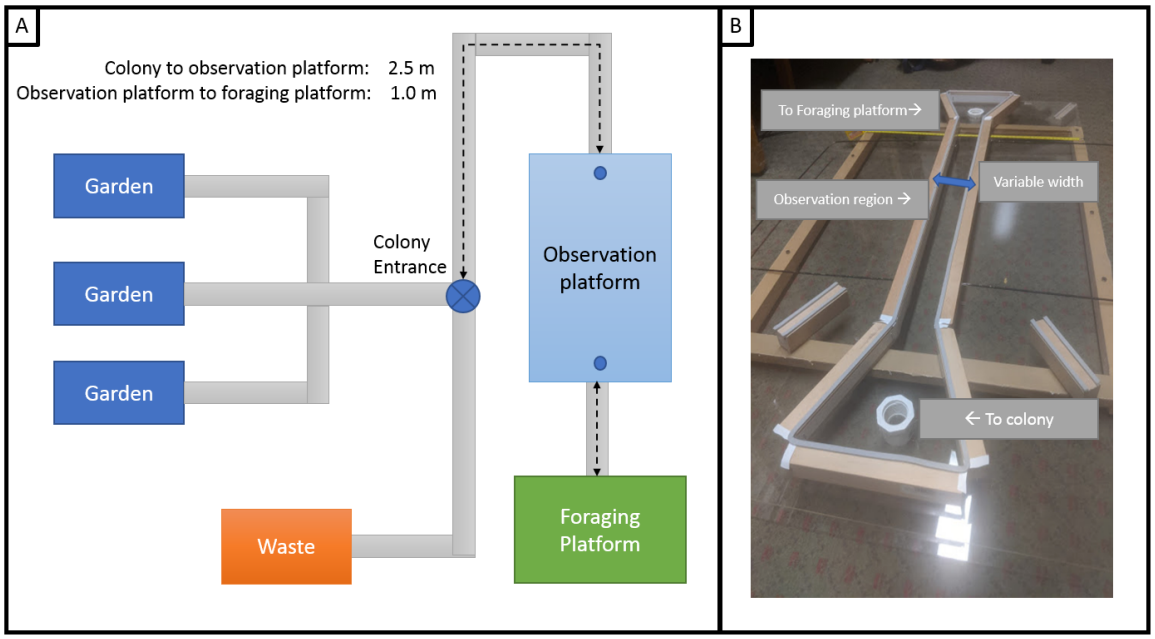

Figure 38. Block diagram of a typical colony layout and location of observation platform, with relevant lengths provided. Diagram not to scale.

Several colonies of the leaf-cutting ant *Atta cephalotes* are maintained for biophysical research at the University of Oregon. The block diagram in figure 38 shows the layout of a typical enclosure. The workers in these highly specialized colonies cut and collect fresh foliage from an isolated feeding platform before transporting it through clear plastic tubing to their symbiotic fungal gardens, as shown schematically in figure 38A. Throughout the experimental period, the colony under study was provided a daily feeding of approximately 100 grams of *Rubus armeniacus*, also known as the Armenian blackberry, collected daily by researchers in our lab. In order to best study the spatial distribution of the ants during these regular foraging periods, the foraging column is routed through an automated observation platform, consisting of

two 2'X4' sheets of clear 1/4" acrylic separated by reposition-able 1 inch talc-coated barriers (shown in figure 38B), with the entire structure supported horizontally above an imaging apparatus. The width of the laterally confined region changes remotely via computer using 4 threaded-shaft stepper motors, allowing accurate and reproducible steric confinement on the time scale of hours to days. On either end of the lower panel, holes act as input and output ports, while a coating of talc and alcohol on the interior vertical surfaces prevents the *A.ceph* from moving vertically up the barriers, effectively restricting foragers to a 2D plane. In practice, long collection times result in a steady wear on the talc layer, and the need to frequently re-apply this preventative must be balanced with minimizing outside interaction during data capture. We minimize variation due to stagnant air, non-uniform pheromone evaporation, and humidity by maintaining a steady rate of air-flow (3 cfm) through the observation chamber. This also serves to prevent the *A.ceph* foragers from utilizing empty space within the observational platform for colony structures like fungus gardens or waste chambers.

In initial experiments, foraging columns clearly avoided the high intensity overhead light utilized for bright-field imaging like that shown in figure 39A. This resulted in a light-induced path bias, especially for experiments in the unconfined limit where the foraging column would slowly drift out of frame. To remove this bias, we switched to dark-field illumination, as shown in figure 39B, and imaged ants using an IR LED strip source (LightingWill). Under these conditions, the path drift observed under

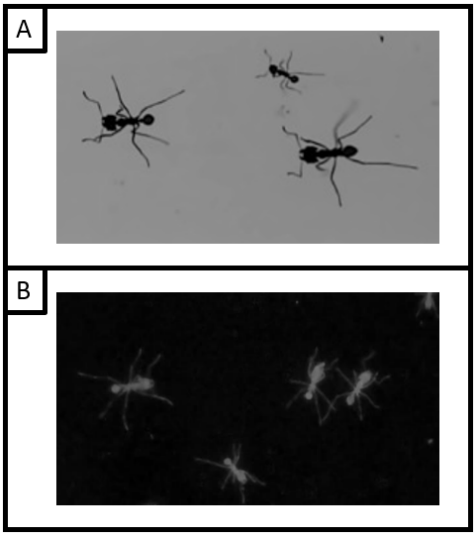

Figure 39. Ant imaging (A) Initial bright-field illumination, visible light (B) Dark-field illumination, IR light

visible light did not occur. This reinforces
literature results showing a reduced sensitivity to longer wavelength light in many ant species [18][19], as well as the demonstrated use of optical cues in the navigation strategies of *Atta cephalotes* [6].

5.2 Data Collection and Analysis

We imaged ant positions and orientations in the foraging column with a Logitech Brio webcam, modified with a near-infrared (LP830) filter and c-mount lens adapter (KuroKesu Inc.) with fixed focus and imaging parameters selected to maximize contrast. Data communication between camera and PC is provided by the OpenCV module in Python. For the results presented in chapter 2 for the unconfined column, each trial consisted of 50 videos collected over 4 days, with each video consisting of 5100 frames collected at 1 FPS, with a spatial resolution of 1920p x 1080p. Between trials the system was removed from the foraging column and cleaned thoroughly with alcohol to prepare for additional data collection. Following each cleaning the ant path was reintroduced to the system with the barriers at a confining width of approximately 5 cm. Once the path had reconnected, the barriers were withdrawn and the path was given approximately 24 hours to stabilize. We include 3 such trials in our analysis. For variable width confinement, one video consisting of 4500 frames is collected at each width during a compression and expansion cycle. This results in 10 videos per cycle (5 expansion and 5 compression), and 50 videos per trial at the same frame-rate and resolution. We clean the system between each collection period as described The results presented in chapter 3 utilize 3 consecutive trials of this type. In total, these results for the unconfined column are extracted from over 750,000 individual frames, while those for the confined column utilize over 2.3 million. In post analysis, each frame is converted to 8-bit monochrome, fish-eye corrected,

and passed through a background removal filter to flatten the image and eliminate temporally persistent (i.e. stationary) features like dropped leaves or barriers, while preserving pixel information about moving ants.

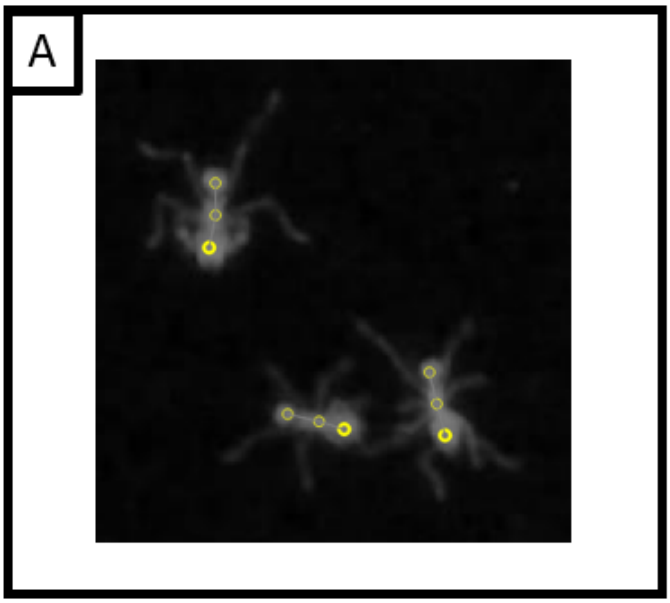

Figure 40. Ant identification and pose estimation via the SLEAP neural net. Yellow dots indicate the positions of the head (bold), thorax, and gaster of each ant.

After image capture and pre-processing, we use the open-source neural net (NN) software SLEAP to quickly and accurately identify ants in individual frames [20]. In order to extract the position and orientation of each ant, our model identifies and reports the position of the head, thorax, and gaster of each ant, as shown in figure 40. From this, we determine the orientation of the vector from gaster to head, and take its midpoint to represent the ants location. We trained this algorithm with a ground-truth human-labeled data set containing $\tilde{2}500$ ants. We estimated the error rate of our current best model based on a sample of $\tilde{4}00$ ants, and find that on average SLEAP is able to correctly identify *A.ceph* foragers 94.6% of the time, with false positive and false negative rates to be 2.2% and 5.8% respectively. This model is also insensitive

to global orientation, with separated error rates for nest-bound and food-bound ants of 94.7% and 94.1%, respectively (see Appendix A). Position and orientation data were analyzed and distilled into lab-frame and ant-frame graphical data via custom Python and Matlab (Mathworks, Inc) scripts. Sample raw data, pre-processing scripts, trained models, sample position data, and python graphical analysis scripts are freely available on FigShare (Kittell, Justin (2023). PRINCIPLES OF TRAFFIC ORGANIZATION IN ANT TRANSPORTATIONNETWORKS. figshare. Dataset. https://doi.org/10.6084/m9.figshare.23808960.v1)

Following the SLEAP identification, the data set is trimmed to remove ants based on bend angles and immobility. Ants found at the same location and orientation across many frames are removed, as well as any found with a head-thorax-gaster angle of $< 90°$.

CHAPTER VI

CONCLUSIONS

Overall, the goal of this project is to increase our understanding of the organizational structures employed by ants like *Atta cephalotes* in hopes that understanding the behavioral rule-sets which tend to produce these structures may help minimize energetic costs in human-engineered systems. To that end, we explored global structure in the lab frame as well as the local structure observed by individual ants over a wide range of confinement levels.

First, our measurements of the mean path width in the unconfined limit yielded a critical length scale for the *A.ceph* foragers. This result provides context for not only our studies of ants under confinement, but also establishes a standard non-dimmensionalized technique for understanding path width in terms of another critical length scale for ant transport networks, ℓ, the average ant length. While the actual width exemplified by any other ant species may differ dramatically from that shown in this work, the similarity in pheremone deposition, transportation, and ant-ant interactions may result in similar paths widths when expressed in the system specific units of ℓ. In future investigations, we will explore this possibility by comparing the organization and fluxes demonstrated by the *A.ceph* with other species and sizes of ants. Other species may be better suited to such investigations as well, given the complexities and challenges associated with leaf-cutter maintenance and observation. If the path widths observed in alternative model systems show path widths near the non-dimmensionalized $W_{path} = 6.7 \pm 2.2$, this length scale may prove to be fundamental for bidirectional auto-chemotactic traffic in the unconfined limit.

Once the statistical properties of the natural path were extracted from forager behavior, we then explore how these measures of organization respond to cyclic

changes in the degree of steric confinement. Under moderate (2.5 – 5.0 cm) and heavy (1.0 – 3.5 cm) confinement, plots of lab frame density, FLDs, FCs, average agent-based densities and tangent-tangent pair correlations all reveal dramatic organizational shifts in response to the decreased lateral extent of the observation region. While not obvious for the unconfined column, the moderately confined path showed clear signatures of a steady state 3 lane traffic pattern. This observation of *Atta cephalotes* behavior stands in contrast with literature results indicating a lack of any organization observed along their foraging routes [10]. This contrast emphasizes the utility of our statistical approach when studying ant traffic, since visually observing structural trends along sparsely populated foraging networks is challenging due to local deviations and low density. We encourage the implementation of similar techniques in future studies of ant traffic. especially when concerned with the emergence and persistence of lanes.

While our investigation into the extremely confined path was hampered by containment limits, our results still displayed a structural transition at a critical width, likely driven by energetic considerations on an individual level. We also observe sharp changes in the symmetry and structure of polar density and TT correlation at these widths resulting from a dynamic transition in behavior triggered by the changing local environmental around each individual. While extracting the details of this behavioral change is still challenging, employing this analysis on a larger scale and over a wider range of environmental restriction may provide a clearer picture of individual behavior and continue to inform our understanding of energetically optimum behavior. Connecting the organizational changes with corresponding changes in these agent based maps provides a link between average local information and global outcomes

in the ant column, and may provide a useful analysis framework for human designed systems experiencing traffic.

Finally, we verified the origin of the observed structural transitions as behavioral, not steric by comparing the statistical lane structures we see in our system with those produced by a 'null' model. Through this method, we emphasize the degree of nematic alignment present in our foraging column, and showcase its consequences in both the lab frame and the ant frame. We also highlight the emergence of lanes in the *A.ceph* foraging column, and show by comparison that the laning signatures described in this study do not emerge as a consequence of ant-wall interactions, but from individual decision making. As described in chapter 3, the models implemented here for ant-wall exclusion do not consider the forward motion and limited turn radius of individual ants when predicting depletion zones. Increasing the complexity of our model from these simplest assumptions will allow us to better fit these depletion zones, and continue to zoom in on how individual decision directly influences the global organization and structure of the foraging column.

Through the data collection protocols and analysis techniques presented herein, we have provided an insight into the organizational strategies and their emergence from individual rule-sets for the ant *Atta cephalotes*, providing key insights into the structure of a biological transport network, as well as a conceptual framework for the design of robust autonomous networks in human transportation systems.

Figure 41. Ant transportation.

APPENDIX

APPENDIX A

A.1 Ant Number Statistics and Total Fluxes

In this section we provide representative plots of average ant number per frame and the frame-wise flux for the experiments described in this work. We assume outgoing food-bound ants count as positive flux, while returning nest-bound ants are counted as negative flux. Each ant's directionality is determined from its lab frame orientation.

A.1.1 The Unconfined Limit

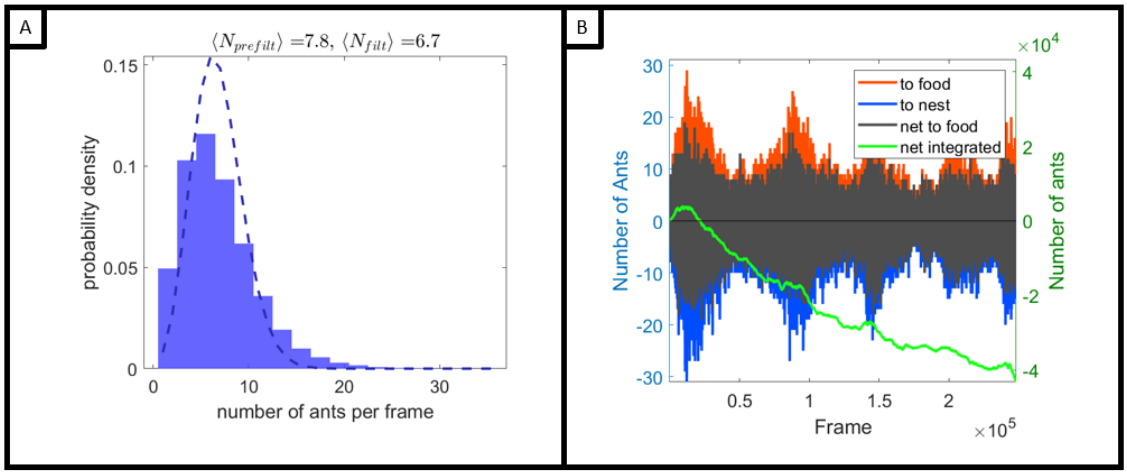

Figure A.42. Ant Number statistics in the unconfined limit. (A) Average ant number is given both before and after filtering (see chapter 5). (B) Ant Flux per frame, showing number of food-bound ants in orange, nest-bound ants in blue, frame-wise net count in black, and net integrated in green.

Figure A.42A shows the normalized probability density for ant number per frame for data collected in the unconfined limit, along with an accompanying Poissonian distribution with the same mean. This comparison reveals that the ant number distribution is not strictly Poissonian under our experimental conditions. Figure A.42B gives the frame-by-frame breakdown of ant flux, as well as the net integrated

ant count. The 250,000 frames represented span 4 days and 4 feeding cycles, evidence of which can seen in variation of net ant number, as pheremone recruitment results in large increases in both positive and negative ant flux. While the net integrated flux for this trial reveals 40,000 more nest bound ants than food bound ants, this is less than 1% of the total number of ants identified.

A.1.2 Moderate and Extreme Confinement

Figure A.43 shows the frame-by-frame ant flux at the minimum and maximum widths under moderate confinement. The average post-filtering ant number for figures A.45A and A.45B are 8.2 and 9.6 respectively. Here, the well defined feeding cycles seen for the unconfined case are not present at either width in figure A.45, since the data set is a composite of samples from many compression and expansion cycles.

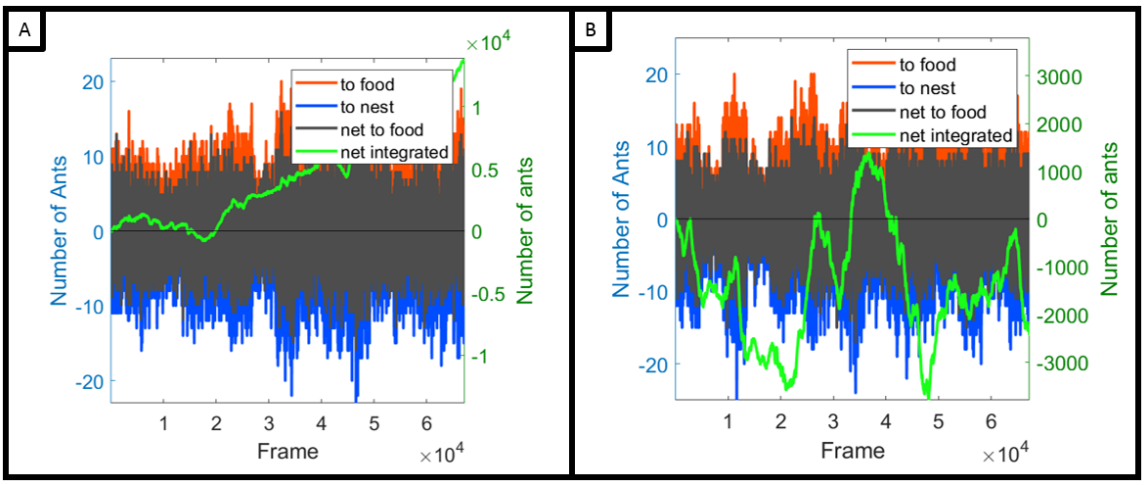

Figure A.43. Representative Ant Fluxes Under Moderate Confinement (A) 5 cm (B) 2.5 cm

Figure A.44 shows the frame-by-frame ant flux at the minimum and maximum widths for the extremely confined case, with representative widths of 2.5 cm and 1.0 cm show in A and B respectively. The average post-filtering ant numbers are 12.0 and 11.3 respectively.

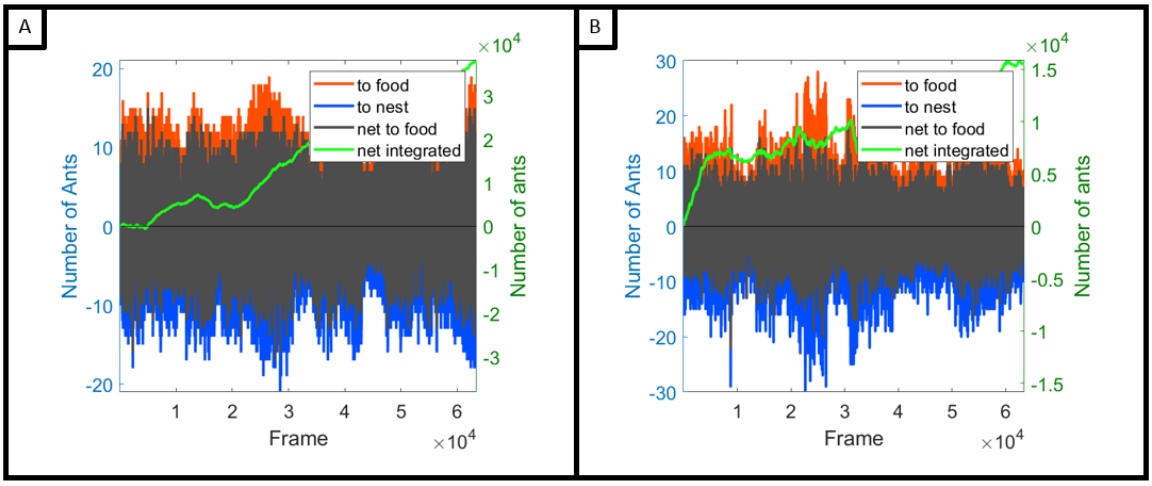

Figure A.44. Representative Ant Fluxes Under Extreme Confinement (A) 2.5 cm (B) 1.0 cm

A.2 Flux Correlate Under Moderate Confinement: All Trials

In figure A.45 we present the complete set of spatial flux correlates (defined in chapter 2) at each moderate confinement level, from 5.0 cm to 2.5 cm. This shows the stability of the observed 3 lane traffic pattern across a wide range of confinement.

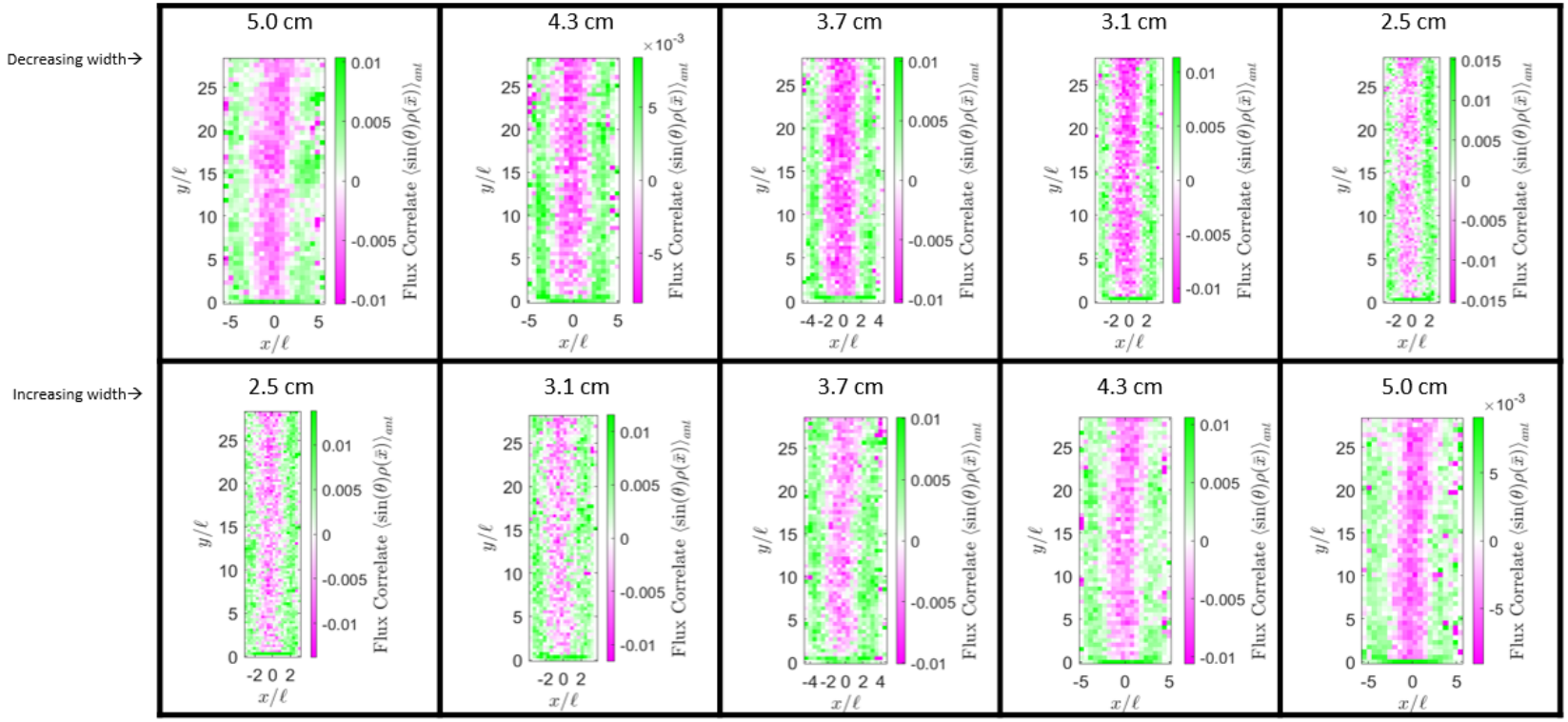

Figure A.45. Flux Correlate at each confinement level: moderate confinement. Color corresponds to lab frame directionality, with magenta being towards the nest, and green being towards the food.

A.3 Neural Net Error Rates

In table A.1 below we show the frame-by-frame breakdown of our SLEAP models neural net error rates. The analysis includes 3 separate videos at different densities, and separates ants by global orientation.

Table A.1. Neural net error rates

(see following)

Neural-net error rates:									
	Food - bound		**Nest - bound**		**Other**				
Frame	in frame	identified	in frame	identified	spurious	total found	total in frame	ratio correct	deviation
1	2	2	0	0	1	2	2	1.000	0.003
2	1	1	3	3	0	4	4	1.000	0.003
3	2	2	1	1	0	3	3	1.000	0.003
4	3	3	2	1	0	4	5	0.800	0.021
5	3	3	2	2	0	5	5	1.000	0.003
6	3	3	1	0	0	3	4	0.750	0.038
7	0	0	2	2	0	2	2	1.000	0.003
8	3	3	2	2	0	5	5	1.000	0.003
9	5	5	3	3	0	8	8	1.000	0.003
10	4	4	1	1	0	5	5	1.000	0.003
11	1	1	3	3	0	4	4	1.000	0.003
12	1	1	3	3	0	4	4	1.000	0.003
13	3	3	4	4	0	7	7	1.000	0.003
14	5	5	2	2	0	7	7	1.000	0.003
15	4	4	3	3	0	7	7	1.000	0.003
16	0	0	5	5	0	5	5	1.000	0.003
17	2	2	4	4	0	6	6	1.000	0.003
18	1	1	1	1	0	2	2	1.000	0.003
19	2	2	1	1	0	3	3	1.000	0.003
20	2	2	3	3	0	5	5	1.000	0.003
21	5	5	4	4	0	9	9	1.000	0.003
22	2	2	8	8	1	10	10	1.000	0.003
23	2	1	4	2	0	3	6	0.500	0.199
24	4	4	4	4	0	8	8	1.000	0.003
25	2	1	1	1	0	2	3	0.667	0.078
26	8	8	8	8	0	16	16	1.000	0.003
27	1	1	2	2	0	3	3	1.000	0.003
28	11	10	8	8	1	18	19	0.947	0.000
29	4	4	3	3	0	7	7	1.000	0.003
30	6	4	7	7	0	11	13	0.846	0.010

Table A.1.

30	6	4	7	7	0	11	13	0.846	0.010
31	7	7	4	2	1	9	11	0.818	0.016
32	5	5	0	0	0	5	5	1.000	0.003
33	4	4	4	4	0	8	8	1.000	0.003
34	2	2	4	4	1	6	6	1.000	0.003
35	5	3	3	2	0	5	8	0.625	0.103
36	3	1	5	5	1	6	8	0.750	0.038
37	3	3	6	6	0	9	9	1.000	0.003
38	5	5	2	2	0	7	7	1.000	0.003
39	6	5	6	6	1	11	12	0.917	0.001
40	4	4	4	4	0	8	8	1.000	0.003
41	6	6	3	3	0	9	9	1.000	0.003
42	5	5	2	2	0	7	7	1.000	0.003
43	5	5	5	5	0	10	10	1.000	0.003
44	5	5	8	8	0	13	13	1.000	0.003
45	4	3	5	4	0	7	9	0.778	0.028
46	2	2	2	2	0	4	4	1.000	0.003
47	9	9	7	7	0	16	16	1.000	0.003
48	4	4	2	1	1	5	6	0.833	0.013
49	7	6	6	5	0	11	13	0.846	0.010
50	3	3	5	5	1	8	8	1.000	0.003
51	3	3	3	3	0	6	6	1.000	0.003
52	3	3	11	10	0	13	14	0.929	0.000
53	2	2	3	3	0	5	5	1.000	0.003
54	7	7	2	2	0	9	9	1.000	0.003
55	4	4	2	2	0	6	6	1.000	0.003
56	4	4	2	2	0	6	6	1.000	0.003
57	1	0	3	3	0	3	4	0.750	0.038
58	5	5	2	2	0	7	7	1.000	0.003
59	3	3	2	2	0	5	5	1.000	0.003
60	3	3	3	3	0	6	6	1.000	0.003
subtotals:	221	208	211	200		408	432	mean dev.	1.21%
percent identified:		94.12%		94.79%			94.59%	plus/minus	11.00%

Table A.1. (cont.)

REFERENCES CITED

[1] J. Toner and Y. Tu, "Flocks, herds, and schools: A quantitative theory of flocking," *Physical Review E* **58** (Oct., 1998) 4828–4858. https://link.aps.org/doi/10.1103/PhysRevE.58.4828. Publisher: American Physical Society.

[2] A. Kotrschal, A. Szorkovszky, J. Herbert-Read, N. I. Bloch, M. Romenskyy, S. D. Buechel, A. F. Eslava, L. S. Alòs, H. Zeng, A. Le Foll, G. Braux, K. Pelckmans, J. E. Mank, D. Sumpter, and N. Kolm, "Rapid evolution of coordinated and collective movement in response to artificial selection," *Science Advances* **6** (Dec., 2020) eaba3148. https://www.science.org/doi/full/10.1126/sciadv.aba3148. Publisher: American Association for the Advancement of Science.

[3] R. W. Garrett, K. A. Carlson, M. S. Goggans, M. H. Nesson, C. A. Shepard, and R. M. S. Schofield, "Leaf processing behaviour in Atta leafcutter ants: 90% of leaf cutting takes place inside the nest, and ants select pieces that require less cutting," *Royal Society Open Science* **3** (Jan., 2016) 150111.

[4] K. Johnson and L. F. Rossi, "A mathematical and experimental study of ant foraging trail dynamics," *Journal of Theoretical Biology* **241** (July, 2006) 360–369. http://www.sciencedirect.com/science/article/pii/S0022519305005278.

[5] S. Mukhopadhyay, M. K. Pathak, and S. Annagiri, "Path minimization in a tandem running Indian ant in the context of colony relocation," *Journal of Experimental Biology* **222** (Nov., 2019) jeb206490. https://doi.org/10.1242/jeb.206490.

[6] K. Vick, "Use of Multiple Cues for Navigation by the Leaf-cutter Ant Atta cephalotes.,". https://drum.lib.umd.edu/handle/1903/2369. Accepted: 2005-08-03T13:37:48Z.

[7] T. Latty, K. Ramsch, K. Ito, T. Nakagaki, D. J. T. Sumpter, M. Middendorf, and M. Beekman, "Structure and formation of ant transportation networks," *Journal of The Royal Society Interface* **8** (Sept., 2011) 1298–1306. https://royalsocietypublishing.org/doi/full/10.1098/rsif.2010.0612. Publisher: Royal Society.

[8] C. R. Reid, D. J. T. Sumpter, and M. Beekman, "Optimisation in a natural system: Argentine ants solve the Towers of Hanoi," *Journal of Experimental Biology* **214** (Jan., 2011) 50–58. https://jeb.biologists.org/content/214/1/50. Publisher: The Company of Biologists Ltd Section: Research Article.

[9] R. J. Mullen, D. Monekosso, S. Barman, and P. Remagnino, "A review of ant algorithms," *Expert Systems with Applications* **36** (Aug., 2009) 9608–9617. https://www.sciencedirect.com/science/article/pii/S0957417409000384.

[10] V. Fourcassié, A. Dussutour, and J.-L. Deneubourg, "Ant traffic rules," *Journal of Experimental Biology* **213** (July, 2010) 2357–2363. https://jeb.biologists.org/content/213/14/2357. Publisher: The Company of Biologists Ltd Section: Commentary.

[11] I. D. Couzin and N. R. Franks, "Self-organized lane formation and optimized traffic flow in army ants.," *Proceedings of the Royal Society B: Biological Sciences* **270** (Jan., 2003) 139–146. https://www.ncbi.nlm.nih.gov/pmc/articles/PMC1691225/.

[12] N. Gravish, G. Gold, A. Zangwill, M. A. D. Goodisman, and D. I. Goldman, "Glass-like dynamics in confined and congested ant traffic," *Soft Matter* **11** (2015) no. 33, 6552–6561. http://xlink.rsc.org/?DOI=C5SM00693G.

[13] L.-A. Poissonnier, S. Motsch, J. Gautrais, J. Buhl, and A. Dussutour, "Experimental investigation of ant traffic under crowded conditions," *eLife* **8** . https://www.ncbi.nlm.nih.gov/pmc/articles/PMC6805160/.

[14] K. A. Bacik, B. S. Bacik, and T. Rogers, "Lane nucleation in complex active flows," *Science* **379** (Mar., 2023) 923–928. https://www.science.org/doi/10.1126/science.add8091. Publisher: American Association for the Advancement of Science.

[15] C. J. Torney, M. Lamont, L. Debell, R. J. Angohiatok, L.-M. Leclerc, and A. M. Berdahl, "Inferring the rules of social interaction in migrating caribou," *Philosophical Transactions of the Royal Society B: Biological Sciences* **373** (May, 2018) 20170385. https://www.ncbi.nlm.nih.gov/pmc/articles/PMC5882989/.

[16] B. Blonder and A. Dornhaus, "Time-Ordered Networks Reveal Limitations to Information Flow in Ant Colonies," *PLOS ONE* **6** (May, 2011) e20298. https://journals.plos.org/plosone/article?id=10.1371/journal.pone.0020298. Publisher: Public Library of Science.

[17] C. P. E. Zollikofer, "Stepping Patterns in Ants: I. Influence of Speed and Curvature," *Journal of Experimental Biology* **192** (July, 1994) 95–106. https://doi.org/10.1242/jeb.192.1.95.

[18] A. Yilmaz and J. Spaethe, "Colour vision in ants (Formicidae, Hymenoptera)," *Philosophical Transactions of the Royal Society B: Biological Sciences* **377** (Sept., 2022) 20210291. https://royalsocietypublishing.org/doi/10.1098/rstb.2021.0291. Publisher: Royal Society.

[19] V. Aksoy and Y. Camlitepe, "Spectral sensitivies of ants – a review," *Animal Biology* **68** (Mar., 2018) .

[20] T. D. Pereira, N. Tabris, A. Matsliah, D. M. Turner, J. Li, S. Ravindranath, E. S. Papadoyannis, E. Normand, D. S. Deutsch, Z. Y. Wang, G. C. McKenzie-Smith, C. C. Mitelut, M. D. Castro, J. D'Uva, M. Kislin, D. H. Sanes, S. D. Kocher, S. S.-H. Wang, A. L. Falkner, J. W. Shaevitz, and M. Murthy, "SLEAP: A deep learning system for multi-animal pose tracking," *Nature Methods* **19** (Apr., 2022) 486–495. `https://www.nature.com/articles/s41592-022-01426-1`. Number: 4 Publisher: Nature Publishing Group.